

**A LYAPUNOV EXPONENT APPROACH FOR IDENTIFYING CHAOTIC
BEHAVIOR IN A FINITE ELEMENT BASED DRILLSTRING VIBRATION
MODEL**

A Thesis

by

KATHIRA MONGKOLCHEEP

Submitted to the Office of Graduate Studies of
Texas A&M University
in partial fulfillment of the requirements for the degree of

MASTER OF SCIENCE

August 2009

Major Subject: Mechanical Engineering

**A LYAPUNOV EXPONENT APPROACH FOR IDENTIFYING CHAOTIC
BEHAVIOR IN A FINITE ELEMENT BASED DRILLSTRING VIBRATION
MODEL**

A Thesis

by

KATHIRA MONGKOLCHEEP

Submitted to the Office of Graduate Studies of
Texas A&M University
in partial fulfillment of the requirements for the degree of

MASTER OF SCIENCE

Approved by:

Co-Chairs of Committee,	Alan B. Palazzolo
	Annie Ruimi
Committee Members,	C. Steve Suh
	Dan Zollinger
Head of Department,	Dennis L. O'Neal

August 2009

Major Subject: Mechanical Engineering

ABSTRACT

A Lyapunov Exponent Approach for Identifying Chaotic Behavior in a Finite Element Based Drillstring Vibration Model. (August 2009)

Kathira Mongkolcheep, B.Eng., Chulalongkorn University, Bangkok, Thailand

Co-Chairs of Advisory Committee: Dr. Alan B. Palazzolo
Dr. Annie Ruimi

The purpose of this work is to present a methodology to predict vibrations of drillstrings for oil recovery service. The work extends a previous model of the drill collar between two stabilizers in the literature to include drill collar flexibility utilizing a modal coordinate condensed, finite element approach. The stiffness due to the gravitational forces along the drillstring axis is included. The model also includes the nonlinear effects of drillstring-wellbore contact, friction and quadratic damping. Bifurcation diagrams are presented to illustrate the effects of speed, friction at wellbore, stabilizer clearance and drill collar length on chaotic vibration response. Their effects shifts resonance peaks away from the linear natural frequency values and influences the onset speed for chaos. A study is conducted on factors for improving the accuracy of Lyapunov Exponents to predict the presence of chaos. This study considers the length of time to steady state, the number and duration of linearization sub-intervals, the presence of rigid body modes and the number of finite elements and modal coordinates. The Poincaré map and frequency spectrum are utilized to confirm the prediction of Lyapunov exponent analysis. The results may be helpful for computing Lyapunov exponents of

other types of nonlinear vibrating systems with many degrees of freedom. Vibration response predictions may assist drilling rig operators in changing a variety of controlled parameters to improve operation procedures and/or equipment.

ACKNOWLEDGEMENTS

I would like to give my sincere gratitude to those that have helped me through my master degree studies.

I especially would like to thank my advisor, Dr. Palazzolo, for his invaluable advice, guidance, and encouragement, as well as consultation throughout the course of my education. I would also like to give my special thanks to Dr. Ruimi for her support, thoughtfulness and kindness to me.

I wish to thank Dr. Suh and Dr. Zollinger for serving on my master committee, and for their useful comments and time. Thanks to all of my friends who have supported me in every way.

Finally, thanks to my mother and father, and my family for their love and encouragement.

NOMENCLATURE

A	Cross-sectional area
$[A]$	Jacobian matrix
C_d	Drag coefficient
$[C]$	Global damping matrix
D_c	Drill collar outside diameter
$E, [E]$	Modulus of elasticity
$F_{b,r}, F_{b,t}$	Normal and tangential contact forces, respectively
F_{d,x_2}, F_{d,x_3}	Linear damping forces in x_2 and x_3 direction, respectively
F_{e,x_2}, F_{e,x_3}	Imbalance forces in x_2 and x_3 direction, respectively
F_{f,x_2}, F_{f,x_3}	Nonlinear damping forces in x_2 and x_3 direction, respectively
$\{F\}$	Force vector
G	Shear modulus
I	Second moment of inertia when taking the symmetry of cross-section
I_{x_2}, I_{x_3}	Second moment of inertia about x_2 and x_3 axes, respectively
$[I]$	Identity matrix
J	Polar area moment of inertia
K_{ii}	Generalized stiffness
K_{S2}, K_{S3}	Shear correction coefficients in x_1 - x_2 and x_1 - x_3 planes, respectively
K_S	Shear correction coefficient when taking the symmetry of cross-

	Section
$[K]$	Global stiffness matrix
$[K_A]$	Axial stiffness matrix
$[K_B]$	Bending stiffness matrix
$[K_G]$	Stress stiffness matrix
$[K_S]$	Shear stiffness matrix
$[K_T]$	Torsional stiffness matrix
$[K_e]$	Element stiffness matrix
L	Drill collar length
M_{ii}	Generalized mass
M_{x_2}, M_{x_3}	Bending moment about x_2 and x_3 axes, respectively
$[M]$	Global mass matrix
$[M_R]$	Rotary inertia matrix
$[M_T]$	Translational mass matrix
$[M_\phi]$	Torsional mass matrix
$[M_e]$	Element mass matrix
N_m	Number of orthonormal modes
N_r	Number of retained mode
N_s	Number of revolutions before calculating Lyapunov exponents
N_t	Number of time intervals in Lyapunov exponent calculation
N_i^k	Distance between linearized solution and nonlinear solution
$[N]$	Shape function matrix

$[N_R]$	Shape function matrix for rotations
$[N_T]$	Shape function matrix for translations
$[N_\phi]$	Shape function matrix for torsion
$[\tilde{P}]$	Modal matrix
T	Total kinetic energy
T_R	Kinetic energy of rotations
T_T	Kinetic energy of translations
T_ϕ	Kinetic energy of torsion
U	Total strain energy
U_A	Axial strain energy
U_B	Bending strain energy
U_G	Stress stiffening strain energy
U_0	Strain energy per unit volume
U_S	Shear strain energy
U_T	Torsional strain energy
V_{x_2}, V_{x_3}	Shear forces along x_2 and x_3 axes, respectively
c_d	Linear damping coefficient
c_f	Nonlinear fluid damping coefficient
e_0	Mass eccentricity
\tilde{f}_i	Modal forces
k_b	Wellbore stiffness

m_e	Unbalanced mass
n_e	Number of differential equations
q_i	Nodal displacement (Physical coordinates)
$\{q\}$	Nodal displacement vector (Physical coordinate vector)
r	Radial displacement
s_0	Clearance between the stabilizer and wellbore
t	Time
u_i	Displacement along x_i axis
$\{u\}$	Displacement vector
u, v, w	Displacements of a point on the mid-plane of an undeformed beam
x_1	Longitudinal axis of the beam (drillstring)
x_2, x_3	Transverse axis of the beam (drillstring)
$\{x\}$	Nonlinear solution
y_i	Modal coordinates
$\{y\}$	Modal coordinate matrix
θ_i	rotation of a transverse normal plane about the x_i axis
Ω	Rotational frequency
μ_b	Wellbore friction coefficient
ρ	Material density
ρ_f	Fluid density
$\{\sigma\}$	Stress
$\{\varepsilon\}$	Strain

α, β	Proportional damping coefficients
λ_i	Eigenvalues
ω_i	Natural frequencies
ω	Whirl speed
$\{\phi\}_i$	Eigenvectors (normal modes)
$\{\tilde{\phi}\}_i$	Orthonormal modes
$[A]$	Eigenvector matrix
ζ_i	Damping ratio
η_i	Linearized solution
$\{\eta\}$	Linearized solution vector

TABLE OF CONTENTS

	Page
ABSTRACT	iii
ACKNOWLEDGEMENTS	v
NOMENCLATURE	vi
TABLE OF CONTENTS	xi
LIST OF FIGURES	xiii
LIST OF TABLES	xv
 CHAPTER	
I INTRODUCTION	1
1.1 Literature review	4
1.2 Statement of thesis	11
1.3 Objectives and organization	11
II BACKGROUND THEORY	13
2.1 Timoshenko beam theory	13
2.2 Force models	17
2.3 Finite element method	19
2.3.1 A three-dimensional finite element	20
2.3.2 Mass matrix	22
2.3.3 Stiffness matrix	23
2.3.4 Damping matrix	26
2.3.5 Equation of motion	27
2.4 Modal approach	27
2.5 Nonlinear dynamics techniques	29
2.5.1 Lyapunov exponents	30
2.5.2 Poincaré map	34
2.5.3 Bifurcation diagram	34
2.5.4 Frequency spectrum	35
III METHODOLOGY	36

CHAPTER	Page
3.1 Model	36
3.2 Finite element method conjunction with a modal method	41
3.3 Nonlinear dynamics analysis.....	43
3.4 Study cases	43
IV RESULTS.....	45
4.1 Convergence studies.....	45
4.2 Model validation	53
4.2.1 Boundary condition.....	53
4.2.2 Software tool.....	57
4.3 The effects of the system parameters on the vibration behavior	58
4.3.1 Nonlinear forces.....	58
4.3.2 Physical parameter effects	59
V CONCLUSIONS	70
REFERENCES.....	73
VITA	78

LIST OF FIGURES

FIGURE	Page
1.1 Major components of the drillstring model.....	2
2.1 Kinematics of the Timoshenko beam theory in the x_1 - x_2 plane	14
2.2 The equilibrium of differential beam in the x_1 - x_2 plane	15
2.3 Kinematics of the Timoshenko beam theory in the x_1 - x_3 plane	16
2.4 The equilibrium of differential beam in the x_1 - x_3 plane	17
2.5 End view of deflected drill collar showing mass eccentricity and contact point	18
2.6 Contact forces on the stabilizer	19
2.7 Nodal displacements for a three-dimensional beam element.....	20
2.8 Sketch of the change in distance between two nearby trajectories	31
2.9 Computer flowchart for Lyapunov exponent calculation.....	33
3.1 Flowchart of methodology in this work	37
3.2 A general drillstring including the drillpipe, drill collar, stabilizers, and drill bit	40
3.3 The finite element model.....	42
4.1 Bifurcation diagrams when using different numbers of modes	47
4.2 Vibrations at drill collar center and stabilizer obtained from full system and reduced system for a non-chaotic response	49
4.3 Vibrations at drill collar center and stabilizer obtained from full system and reduced system for a chaotic response	50
4.4 Maximum Lyapunov exponent convergence with time for a non-chaotic and a chaotic response.....	52

FIGURE	Page
4.5 Five lowest mode shapes of the drill collar–stabilizer model	54
4.6 Vibrations at the drill collar center and stabilizer, with and without the drillpipe, for a non-chaotic rpm.....	55
4.7 Vibrations at the drill collar center and stabilizer, with and without the drillpipe, for a chaotic rpm	56
4.8 Maximum off-diagonal term in the identity matrix versus time intervals .	58
4.9 Bifurcation diagrams showing the influence of nonlinear forces on chaotic vibrations	60
4.10 Bifurcation diagrams for model with different coefficients of friction.....	61
4.11 Maximum Lyapunov exponent versus drillstring rpm with different coefficients of friction	62
4.12 Bifurcation diagrams for model with different lengths of drill collar section.....	64
4.13 Bifurcation diagrams when varying stabilizer clearance	65
4.14 Maximum Lyapunov exponent versus drillstring rpm when varying stabilizer clearance	66
4.15 Vibration response and nonlinear dynamics analysis for a non-chaotic rpm.....	68
4.16 Vibration response and nonlinear dynamics analysis for a chaotic rpm	69

LIST OF TABLES

TABLE	Page
3.1 Parameters used in the simulations	39
4.1 The first ten natural frequencies of the model.....	46
4.2 The chaos onset speed when varying number of modes	48
4.3 Maximum Lyapunov exponents for different times to steady state	51
4.4 Maximum Lyapunov exponents obtained from different numbers of time intervals	51
4.5 Maximum Lyapunov exponents obtained from varying the time interval duration.....	52
4.6 Free–free natural frequencies of drill collar-stabilizer model	53
4.7 The lowest natural frequencies obtained from the analytical solution and the developed software	57
4.8 The chaos onset speed when varying the length of the drill collar	63

CHAPTER I

INTRODUCTION

High demand for energy has forced the oil and gas industry to seek improved methods to increase productivity. Preventing or reducing failures during drilling can significantly reduce cost and air pollution by eliminating equipment replacement, repeated drilling of wells and unnecessary down time. Failures are quite often associated with severe vibrations of the lower part of the drillstring called the bottom-hole-assembly (BHA) due to the interaction between the rotating drillstring and rock formation or surrounding water and drilling mud.

Typically, a drillstring is composed of a hoisting and turning mechanisms (draw work, kelly or top drive), a drillpipe, drill collars, stabilizers and a drill bit. Drill collars are thick-walled, large diameter pipes which provide the weight on bit (WOB) and prevent drill pipes from buckling by keeping them in tension at the surface. Stabilizers (centralizers) are located along the drill collars and above the drill bit, in the lower part of the drillstring known as the bottom hole assembly (BHA). The stabilizers have short sections and a diameter near that of the borehole (or wellbore) to help to center the BHA. They also improve the drill bit performance by preventing bending of the lower part of the drill collar [1, 2, 3]. Figure 1.1 depicts a truncated length of drillpipe (top), a string of

This thesis follows the style of *Journal of Vibration and Acoustics*.

drill collars with two end stabilizers, the BHA and the drill bit. Interactions of the drillstring and the drilling fluid (mud), contact forces between the wellbore and drillstring and interaction between the borehole and the drill bit may cause severe vibrations that can damage the drilling equipment, the drillstring and/or the stabilizers.

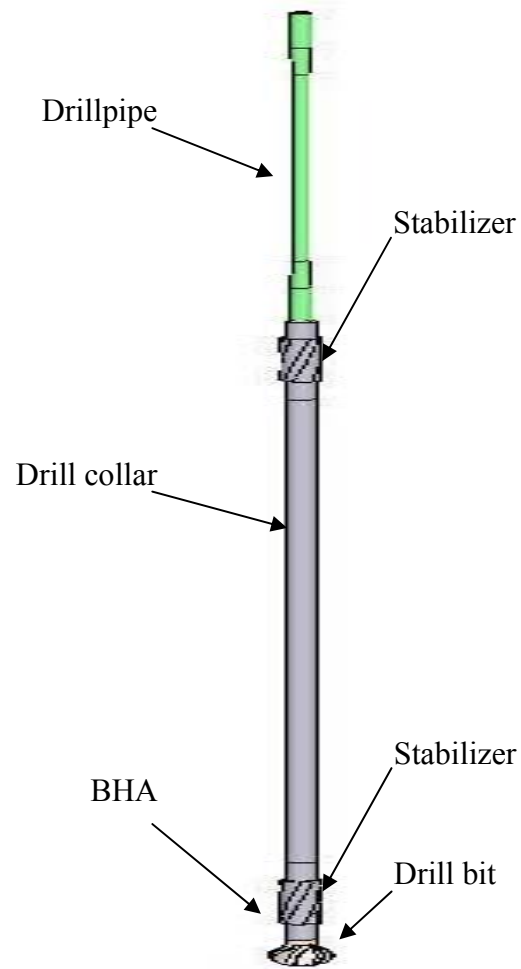


Figure 1. Major components of the drillstring model.

Three types of vibrations are predominant in drilling [4, 5]. Axial vibrations results from interactions between the bits and the hole bottom. This may result in large fluctuations of WOB and suspended particulate phase, erratic rate of penetration (ROP), shaking of surface equipment at shallow drilling depths, loss of tool face and poor directional control. Torsional vibration results from drill collar resonance, bit chatter, stick-slip interaction between the bit and formation and modal coupling. Severe stick-slip motion may even cause a stopping or reversing of the bit direction. Lateral vibrations are called whirling motion and results from interactions between the bits and formation, mass imbalance, bit whirl, and from fluid forces around the drillstring. Lateral vibrations also result from coupling between the lateral. A drillstring can vibrate in any or all of these types and experience failures as indicated by reduction in the rate of penetration and drillstring or bit damage.

This work focuses on predicting lateral chaotic vibrations that result from imbalance, stabilizer borehole impacts and friction, and nonlinear damping. A lateral degree of freedom is assumed at the bit. This is a reasonable assumption because of oversize cutting (bit walk, runout, and formation swell compensation) which leaves a clearance between the bit-through diameter and the as drilled gage hole. A Timoshenko beam based finite element code is employed to model the drillpipe and the drill collars between two stabilizers. Modal condensation is utilized to reduce the number of degrees of freedom and computational time. The vibration response is categorized by the use of nonlinear dynamics techniques which include Lyapunov exponents, bifurcation diagrams and Poincare maps. Lyapunov exponents provide a measure of divergence or

convergence of nearby trajectories and are calculated from the modal coordinate responses as an indication of chaotic vs. non-chaotic behavior. Chaotic motion must produce at least one positive Lyapunov exponent, hence it is sufficient to determine only the maximum Lyapunov exponent. The proposed model includes mass eccentricity, fluid damping, Coulomb friction and stress stiffening due to the axial load from the drill collar weight.

Vibration response predictions may assist drilling rig operators in changing a variety of controlled parameters such as rotary speed, drilling mud composition, stabilizer gaps, drill collar length, etc. This will ultimately lead to improved procedures for oil and gas recovery, a decrease in equipment failure, cost savings and reduced emissions.

1.1 Literature review

Most of the drillstring vibration literature focuses on models of parts or components of the entire drilling rig. Boundary conditions are assumed to facilitate these partial system models. These models are utilized to help explain direct, or indirect (damage) measurements of drillstring vibration.

Lin et al. [6] proposed a single-degree-of-freedom torsional model including the effect of dry friction. The dry friction coefficient decreases with angular velocity from its static value and asymptotically approaches a constant kinetic value at infinite angular velocity. The self-excited stick-slip oscillations yielded by the model showed good qualitative agreement with field measurements. Brett [7] concluded that the drilling

characteristics of the polycrystalline diamond compact (PDC) bits itself can cause severe torsional vibrations. The torsional vibrations result from a reduction in torque when rotary speed increases. He showed that the torsional vibrations are more severe when applying higher WOB, dull bits and at lower rotary speed. Cull and Tucker [8] investigated two different representations of Coulomb friction in a torsional drillstring model: a piecewise friction profile and a continuous and smooth nonlinear friction profile. The comparisons showed that both profiles gave acceptable alternatives for their model. They also indicated that the effect of the viscous damping could slightly reduce the duration of the BHA for both friction profiles. Mihajlović et al. [4] utilized the Coulomb friction to the top drive and Humped friction to the BHA and drill bit. An experimental drillstring setup was also built to compare the results obtained from the simulation. The bifurcation diagrams showed the changes from equilibrium points to limit cycling in which some regions are referred to as stick-slip oscillations. A comparison of numerical and experimental bifurcation diagrams indicated the predictive quality of the model. Navarro-López and Cortés [9] used lumped-parameter torsional model to study the stick-slip oscillations. The model included four elements: top drive, drill pipes, BHA and the drill bit. It also considered the increase in length of drillstring while drilling. The viscous damping torque and the discontinuous dry friction torque were applied at the drill bit. They utilized Hopf bifurcations to extract the parameters that yield non-desired torsional oscillations.

Lateral vibrations, also referred as whirling motion, were analyzed as rotor dynamics by Jansen [10]. A two-degree-of-freedom rotordynamic “Jeffcott Rotor”

model was developed for a drill collar section between two stabilizers, the later modeled as bearings. Nonlinearity was accounted for the drilling fluid, stabilizer clearance and stabilizer-borehole friction. The study showed the results of these effects to the whirl amplitude, the critical speed and the stability. The obtained simulations explained the results from field measurements or from the large-scale multi-degree-of-freedom computer simulation. Van der Heijden [11] utilized the two degree of freedom model of Jansen [9] to analyze the response for chaos with nonlinear dynamics techniques. The bifurcation diagram was used to show the change of responses when varying frequency ratios. Also the response was confirmed by the Poincaré section, frequency spectrum, Lyapunov exponents and the fractal dimension. The study found several instabilities and types of motion, including quasi-periodic and chaos, resulting from many conditions. Kotsonis and Spanos [12] proposed the model describing lateral vibrations of the BHA. The effects of fluid damping, wall contact, mass eccentricity, initial curvature of drill collar and also linear and parametric coupling between axial force and lateral vibration were considered. When the coupling was not included, the drill collar stabilized at a constant radius. When coupling was taken into account, chaotic motion resulted. Whether the system was chaotic or random was tested by using the minimum phase-volume deconvolution technique.

In the above studies, the drillstring vibrations occur at a single mode but they can also be coupled. Such as the case in Yigit and Christoforou [13] utilized a lumped parameter model to investigate coupled torsional-lateral vibrations. The model included the effects of the rotary drive system, the impacts of collars with the borehole and the bit

rotation-dependent weight and torque on bit. The obtained stick-slip results were in close qualitative agreement with the field measurements. The active controller was also studied and could show good results in removing the stick-slip oscillations. Leine et al. [5] modeled oil well drillstring vibration with sub-system models for stick-slip motion and for whirl motion. Their work showed that increasing the rotary speed will result in a change from stick-slip to whirl motion as evidenced by downhole measurements. However there was no clear evidence that decreasing the rotary speed would result in a reversal of the motion from whirl to stick-slip motion. This behavior was explained by the presence of multiple stable solutions on the bifurcation diagrams. Yigit and Christoforou [14] employed an Euler-Bernoulli beam, assumed modes model to study the coupling of axial and lateral vibrations. The impact of the drillstring with the borehole wall was modeled using Hertzian contact theory. The coupling of the vibrations yielded a value of the critical axial load lower than the one obtained from a linear analysis and resulted in chaotic response.

Richard et al. [15] studied the coupling between the torsional and axial vibrations modes resulting from the bit-rock interaction. Their model considered only the inertial moment of BHA and showed the existence of self-excited vibrations characterized by stick-slip oscillation or bit bouncing. It was shown that the fundamental source of the self excitation (instability) was the lag of the cutting force and torque behind the penetration rate. Their work was extended by Zamanian et al. [16] who took into account the rotation of the rotary table, active damping at the top and damping of the drilling mud. Unlike the Richard et al. conclusions, they indicated that the system could always

be stable by an appropriate selection of system parameters, and showed that stick-slip vibrations could be observed from the amplitude of the oscillations of the rotary table. Yigit and Christoforou [17] investigated the coupled torsional and axial vibrations at the drill bit through the relation of weight-on-bit, torque-on-bit and cutting condition. Their model included the rotary table driven by an armature controlled dc motor through a gearbox. To suppress stick-slip vibrations and bit-bounce effectively, the study showed that the model should have both the feedback and active controller. The effect of torsion in drillstring on the stability and on the axial and torsional loads was investigated by Elsayed et al. [18]. A lump-parameter model was used and a mode summation method was applied to reduce the order of the system. The study of frequency spectrum gave the better insight of the torsional effect. The study showed the importance of including the torsional effect in the drillstring analysis to make more accurate results.

The full coupling of axial, lateral and torsional vibrations using a lumped parameter model was studied by Christoforou and Yigit [19]. The mutual dependence of these vibrations arose from bit-formation and drillstring-borehole interactions as well as other geometric and dynamic nonlinearities. The contact with the borehole was analyzed by using the momentum balance method. The stick-slip and bit-bounce simulations agreed well with field observations. In addition, they designed an active controller which was effective in reducing these oscillations.

Melakhessou et al. [20] studied on the contact zone of the BHA and characterized it into two sections: one centered on the axis of the well and one related to the first by the flexible string. The four-degree-of-freedom model included the effects of

bending and torsion, the whirling motion as well as Coulomb friction between a tool-joint and borehole and the drillstring and borehole. Simulation results agreed well with those obtained with an experimental set-up and showed that their model was accurate enough to simulate the local contact between the drillstring and the borehole.

The response of drag bits (or PDC bits) was investigated by Detournay and Defourny [21]. Their model accounted for both rock cutting processes and frictional contact between the cutter wearflats and the rock. The model also showed the relations between weight-on-bit, torque, angular velocity and rate of penetration.

Jogi et al. [22] determined the natural frequencies of the axial, torsional and lateral vibrations of the BHA. The simulation results obtained with in-house models agreed well with field data obtained with downhole vibration measurement sensors.

The finite element method has also been used for the analysis of the drillstring vibrations. The drillstring with the roller cone bit utilizing a finite element method was analyzed by Spanos et al. [23]. The model considered the formation surface profile and torque-on-bit specified for the roller cone bit. The results indicated that the rotary speeds corresponding to axial natural frequencies were critical speeds causing wide fluctuation of the weight-on-bit. The very high rotary speed could cause the bit to lift off and the WOB to drop. Spanos et al. [24] employed an Euler Bernoulli, based finite element model to simulate the BHA vibrations under monochromatic harmonic excitation. The effect of axial force on the lateral vibration, damping as a function of mud density and vibration frequency and the added mass of the drilling fluid were accounted for in their model. In this study the response was found by the use of a transfer function

representation by modal superposition and iterative techniques while considering the frequency-dependent added mass. This method allowed addressing the nonlinearity of the wellbore contact. Khulief et al. [25] modeled the drillstring including the drillpipe and drill collars using Euler-Bernoulli beam theory. The governing equations were derived using a Lagrangian approach and accounted for the torsional-lateral inertia coupling, the axial-lateral geometric nonlinear coupling, the gyroscopic effect, and the stick-slip interaction forces. Unlike in other studies, the effect of the gravitational force field was also considered in this study. The effect of gravitation, generally ignored in other studies was also considered by splitting the drillstring into two sections: one in tension above the neutral point and one in compression below the neutral point. The order of the system was reduced using a modal transformation method. Transient responses resulting from various excitations were used to validate the model. Results indicated that lateral excitations affected axial and torsional vibrations and that frictional torque caused stick-slip oscillations.

This work extends the work of Jansen [10] and Van der Heijden [11] who analyzed the lateral vibrations of the drill collar and BHA, including stabilizers at both ends. Our contributions include modeling of drill collar flexibility utilizing finite elements and modal coordinate reduction, characterization of chaos with Lyapunov exponents and a strange attractor map, and consideration of the effects of friction, drill collar length and stabilizer clearance on chaotic vibration. The upper boundary condition employed by Jansen [10] and Van der Heijden [11] is also validated by comparing responses with and without the drillpipe. A study of parameter variation for computing

the Lyapunov exponents of a larger order model is included and may provide a guide for studies of chaos in other types of vibrating systems.

1.2 Statement of thesis

The thesis of this work is that Lyapunov exponents can be calculated for a finite element based model of a drillstring and provide a quantitative indicator of chaotic and non-chaotic behavior. An in-house software is developed for a Timoshenko beam, finite element representation of a drillstring model. The modal method is employed to increase the efficiency of the computations. Post processing software for characterizing the vibration behavior from the modal coordinates is then developed by the use of nonlinear dynamics techniques including Lyapunov exponents.

1.3 Objectives and organization

In this study, our objectives are as follows:

- 1) To develop and validate a finite element software for simulating the drillstring vibrations
- 2) To investigate the behavior of drillstring vibrations from the finite element model
- 3) To understand the effect of the system parameters to the system response
- 4) To develop a computationally efficient and reliable approach for identifying chaotic behavior on a drillstring model

The background theory is provided in Chapter II. The methodology used for this work is described in Chapter III. All study results and vibration response are shown and analyzed by nonlinear dynamics techniques in Chapter IV. The summary and conclusion as well as recommendations for future work are given in Chapter V.

CHAPTER II

BACKGROUND THEORY

In this chapter, we briefly summarized the relevant theories required in modeling and analysis of our study. The drillstring is modeled using Timoshenko beam finite elements theory to describe lateral vibrations. The system equation of motion is derived by Lagrangian method. The beam stiffness also includes stress stiffening due to the gravitational force acting along the beam axis. The chaotic vibrations are predicted to result from imbalance, stabilizer wellbore impacts and friction, and nonlinear damping. A modal condensation approach is utilized to reduce the number of degrees of freedom of the finite element system and computational time. Lastly, nonlinear response behavior is then categorized by the use of nonlinear dynamics techniques including Lyapunov exponents, bifurcation diagram, Poincaré map and frequency spectrum.

2.1 Timoshenko beam theory

The Euler-Bernoulli beam theory assumes that plane cross sections perpendicular to the axis of the beam remain plane and normal to the longitudinal axis after deformation. In Timoshenko beam theory (TBT), the first assumption is kept but the normality condition is relaxed by assuming that the rotation of a transverse normal plane about the x_3 -axis (θ_3) is not equal to $-dv/dx_1$ (see Fig. 2.1). Therefore, the transverse shear deformation is not zero [26]. Let the longitudinal axis of the beam lie on a local x_1 axis, the kinematics of the TBT in the x_1 - x_2 plane is shown in Fig. 2.1.

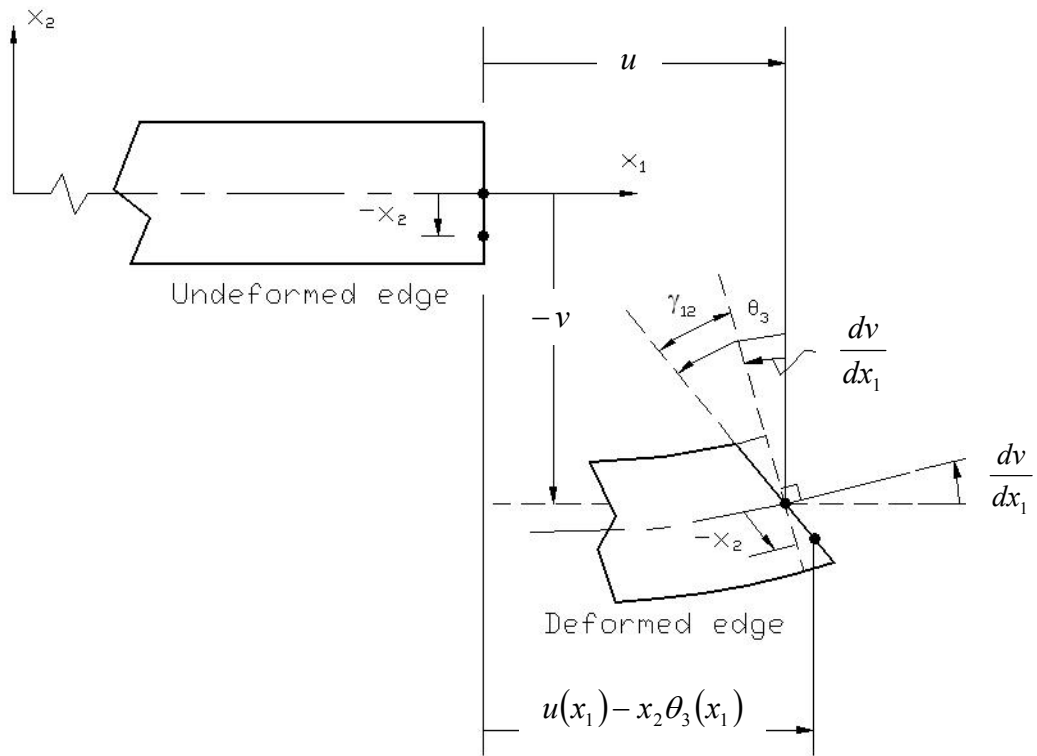


Figure 2.1. Kinematics of the Timoshenko beam theory in the x_1 - x_2 plane [26].

The displacement field of the beam in the TBT in the x_1 - x_2 plane can be expressed as

$$u_1 = u(x_1) - x_2 \theta_3(x_1), \quad u_2 = v(x_1), \quad u_3 = 0 \quad (2.1)$$

where (u_1, u_2, u_3) are the displacements of a point along the (x_1, x_2, x_3) coordinates (u, v) are the displacements of a point on the mid-plane of an undeformed beam in (x_1, x_2) directions, and θ_3 is the angle about the x_3 -axis of a transverse straight line. The equilibrium of the differential length beam subjected to shear forces V_{x_2} and bending moments M_{x_3} is shown in Fig. 2.2. The equilibrium equations of the TBT are

$$\frac{dV_{x_2}}{dx_1} = 0, \quad \frac{dM_{x_3}}{dx_1} + V_{x_2} = 0,$$

$$M_{x_3} = EI_{x_3} \frac{d\theta_3}{dx_1}, \quad V_{x_2} = K_{S2} GA \left(-\theta_3 + \frac{dv}{dx_1} \right) \quad (2.2)$$

where E is the modulus of elasticity, I_{x_3} is the second moment of inertia about the x_3 -axis, K_{S2} is the shear correction coefficient in x_1 - x_2 plane, G is the shear modulus and A is the cross-sectional area.

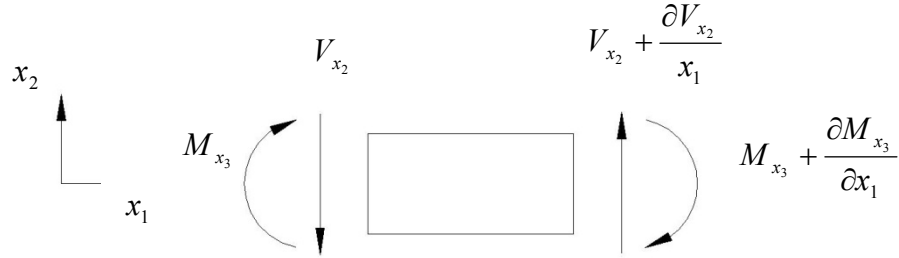


Figure 2.2. The equilibrium of differential beam in the x_1 - x_2 plane.

Similarly, the kinematics of the TBT in the x_1 - x_3 plane is shown in Fig. 2.3 and the displacement field is

$$u_1 = u(x_1) + x_3 \theta_2(x_1), \quad u_2 = 0, \quad u_3 = w(x_1) \quad (2.3)$$

where w is the displacement of a point on the mid-plane of an undeformed beam in x_3 direction, and θ_2 is the angle about the x_2 -axis of a transverse straight line.

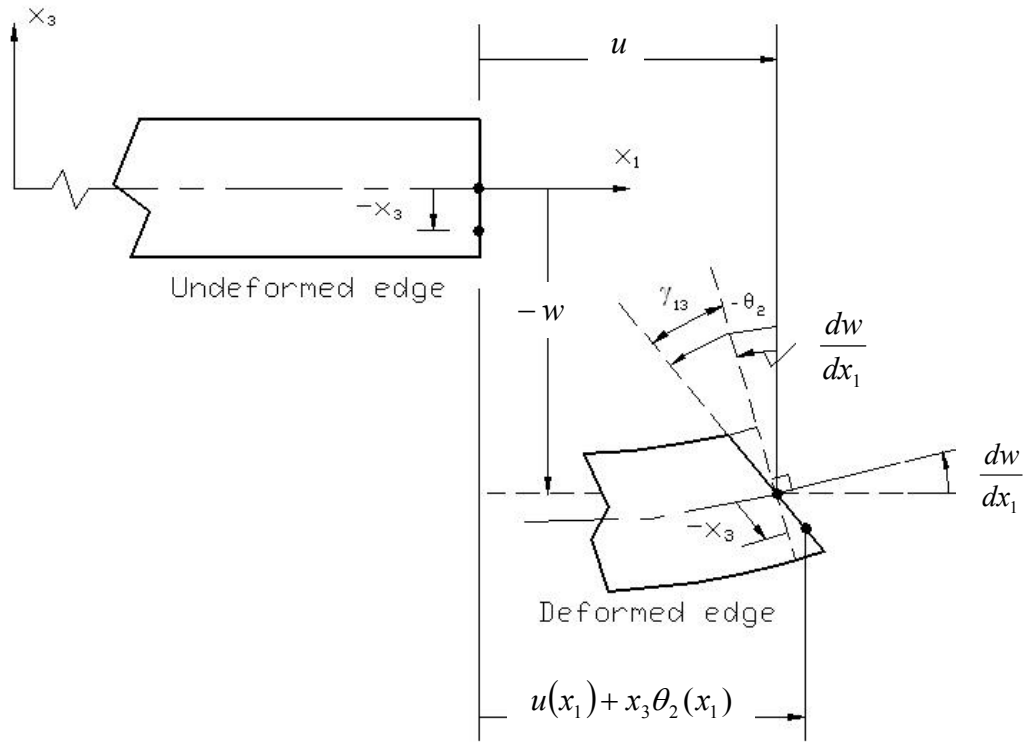


Figure 2.3. Kinematics of the Timoshenko beam theory in the x_1 - x_3 plane [26].

The equilibrium of the differential length beam subjected to shear forces V_{x_3} and bending moments M_{x_2} as shown in Fig. 2.4 is

$$\frac{dV_{x_3}}{dx_1} = 0, \quad -\frac{dM_{x_2}}{dx_1} + V_{x_3} = 0, \quad (2.4)$$

$$M_{x_2} = EI_{x_2} \frac{d\theta_2}{dx_1}, \quad V_{x_3} = K_{S3} GA \left(\theta_2 + \frac{dw}{dx_1} \right)$$

where I_{x_3} is the second moment of inertia about the x_2 -axis, K_{S3} is the shear correction coefficient in x_1 - x_3 plane and E , G and A are as described previously.

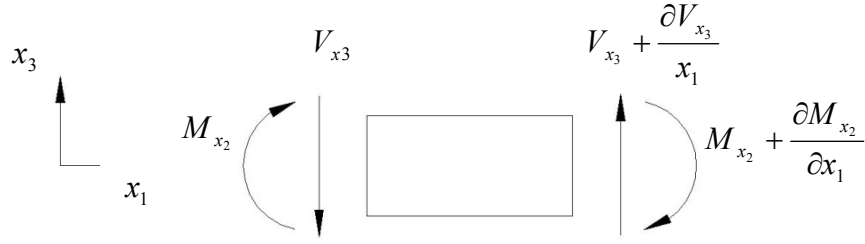


Figure 2.4. The equilibrium of differential beam in the x_1 - x_3 plane.

2.2 Force models

The imbalance force due to mass eccentricity, e_0 , can be expressed in rectangular coordinates (x_2, x_3) as

$$F_{e,x_2} = m_e \Omega^2 e_0 \cos(\Omega t), \quad F_{e,x_3} = m_e \Omega^2 e_0 \sin(\Omega t) \quad (2.5)$$

where t is time, m_e is the unbalanced mass and Ω is the rotational frequency as shown in Fig. 2.5. A nonlinear damping force due to the vibration of the drill collar in the surrounding mudflow is modeled as a velocity squared proportional force in the direction opposite to the velocity of the drill collar and applied at the midspan location of the drill collar [10, 11]:

$$F_{f,x_2} = -c_f \sqrt{x_2^2 + x_3^2} \dot{x}_2, \quad F_{f,x_3} = -c_f \sqrt{x_2^2 + x_3^2} \dot{x}_3 \quad (2.6)$$

c_f is the equivalent fluid damping coefficient and given in [29] as

$$c_f = \rho_f C_d D_c L / 2 \quad (2.7)$$

where ρ_f is the fluid density, C_d is the drag coefficient, D_c is the collar outside diameter and L is the collar length. Linear damping forces are included at each stabilizer

$$F_{d,x_2} = -c_d \dot{x}_2, F_{d,x_3} = -c_d \dot{x}_3 \quad (2.8)$$

where c_d is the damping coefficient. The linear damper model is employed due to the much smaller clearance at the stabilizers (centralizers). Gyroscopic torque is neglected due to the very low speed of the drillstring.

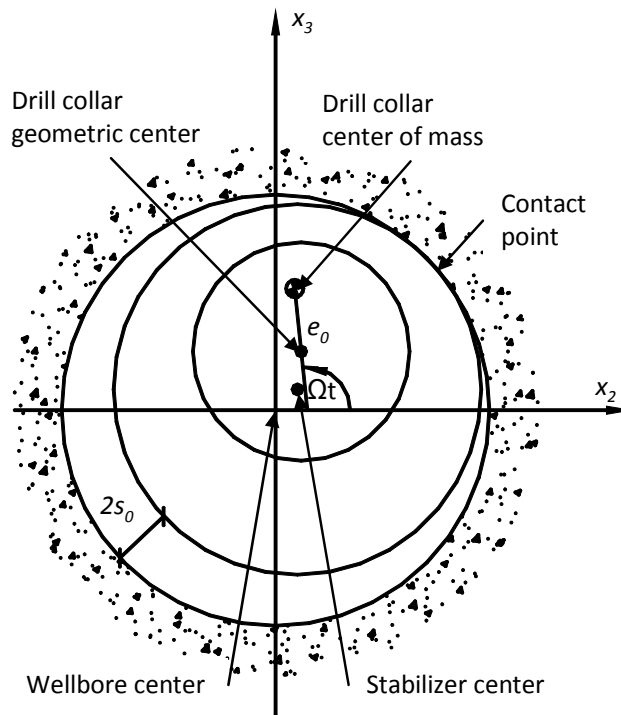


Figure 2.5. End view of deflected drill collar showing mass eccentricity and contact point [10].

Normal and tangential contact forces occur between the stabilizer and wellbore when the lateral displacement of the stabilizer becomes larger than the clearance, $r > s_0$ (Fig. 2.6).

The normal contact force ($F_{b,r}$) is modeled as a linear spring with stiffness, k_b .

$$F_{b,r} = \begin{cases} 0 & , r < s_0 \\ k_b(r - s_0), & r > s_0 \end{cases} \quad (2.9)$$

The tangential, coulomb friction contact force is given by

$$F_{b,t} = \mu_b \text{sign}(\varpi) F_{b,r} \quad (2.10)$$

where ω is the whirl speed and μ_b is the coefficient of friction. The stabilizer section is assumed to always slip when it contacts the wall.

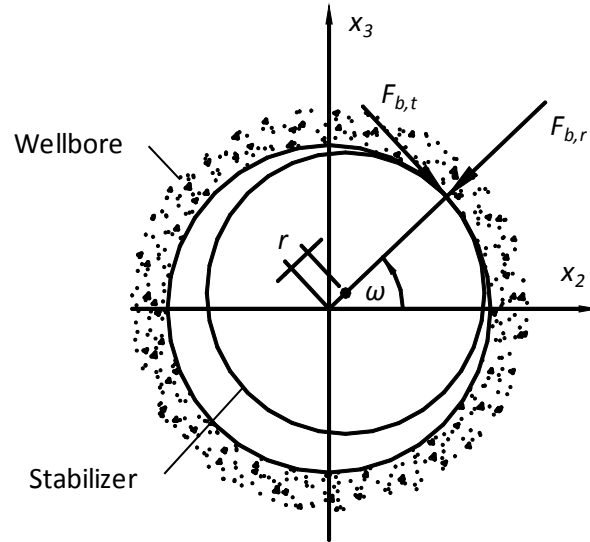


Figure 2.6. Contact forces on the stabilizer [10].

2.3 Finite element method

We used a three-dimensional finite element to discretize the beam. The system equation of motion is derived using a Lagrangian approach. The finite element mass matrices are derived using the kinetic energy. The finite element stiffness matrices are derived using

the elastic strain energy. The proportional damping is employed to represent the viscous damping in a beam. The finite element method was discussed in detail elsewhere [26, 27].

2.3.1 A three-dimensional finite element

An element consists of two nodes at its ends. Each node has six degrees of freedom consisting of three translations (u_1, u_2, u_3) and three rotations ($\theta_1, \theta_2, \theta_3$). The displacement vector of an element can be expressed as

$$\{u\} = [u_1 \quad u_2 \quad u_3 \quad \theta_1 \quad \theta_2 \quad \theta_3]^T \quad (2.11)$$

where $[\]$ is denoted as a row vector. Figure 2.7 shows an element with the nodal displacements. The axis of the beam lies on a local x_1 -axis. The vector of nodal displacements for this element can be expressed as

$$\{q\} = [q_1 \quad q_2 \quad q_3 \quad q_4 \quad q_5 \quad q_6 \quad q_7 \quad q_8 \quad q_9 \quad q_{10} \quad q_{11} \quad q_{12}]^T \quad (2.12)$$

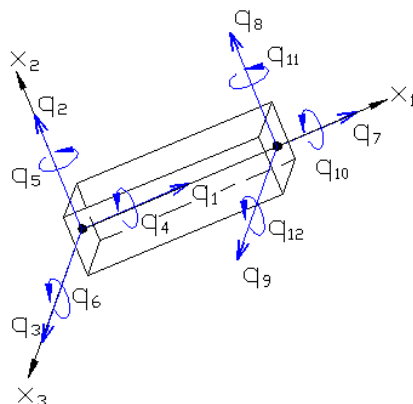


Figure 2.7. Nodal displacements for a three-dimensional beam element.

Let the interpolated forms of the displacements be

$$\{u\} = [N]\{q\} \quad (2.13)$$

where $[N]$ is the shape function matrix of the three-dimensional finite element. The translational deformations, rotations and torsional deformations of an element can be represented in terms of shape functions as follows:

Translations

$$\begin{aligned} \begin{Bmatrix} u_1(x_1) \\ u_2(x_1) \\ u_3(x_1) \end{Bmatrix} &= \begin{bmatrix} N_{Ta1} & 0 & 0 & 0 & 0 & 0 & N_{Ta2} & 0 & 0 & 0 & 0 & 0 \\ 0 & N_{Tb1} & 0 & 0 & 0 & N_{Tb2} & 0 & N_{Tb3} & 0 & 0 & 0 & N_{Tb4} \\ 0 & 0 & N_{Tb1} & 0 & -N_{Tb2} & 0 & 0 & 0 & N_{Tb3} & 0 & -N_{Tb4} & 0 \end{bmatrix} \{q\} \\ &= \begin{bmatrix} N_{Tu_1} \\ N_{Tu_2} \\ N_{Tu_3} \end{bmatrix} \{q\} = [N_T]\{q\} \end{aligned} \quad (2.14)$$

where N_T is the shape function matrix for translation, and a and b are denoted as axial and bending, respectively.

Rotations

$$\begin{aligned} \begin{Bmatrix} \theta_2(x_1) \\ \theta_3(x_1) \end{Bmatrix} &= \begin{bmatrix} 0 & N_{Rb1} & 0 & 0 & 0 & N_{Rb2} & 0 & N_{Rb3} & 0 & 0 & 0 & N_{Rb4} \\ 0 & 0 & -N_{Rb1} & 0 & N_{Rb2} & 0 & 0 & 0 & -N_{Rb3} & 0 & N_{Rb4} & 0 \end{bmatrix} \{q\} \\ &= \begin{bmatrix} N_{R\theta_2} \\ N_{R\theta_3} \end{bmatrix} \{q\} = [N_R]\{q\} \end{aligned} \quad (2.15)$$

where N_R is the shape function matrix for rotation.

Torsion

$$\begin{aligned} \{\theta_1(x_1)\} &= [0 \ 0 \ 0 \ N_{\phi_1} \ 0 \ 0 \ 0 \ 0 \ 0 \ 0 \ N_{\phi_2} \ 0 \ 0] \{q\} \\ &= [N_\phi] \{q\} \end{aligned} \quad (2.16)$$

where N_ϕ is the shape function matrix for torsion.

2.3.2 Mass matrix

The element mass matrices are obtained from the kinetic energy. For the small vibrations, the kinetic energy of translations and rotations can be written as

Translations

$$T_T = \frac{\rho A}{2} \int_0^L \left\{ \left(\frac{\partial u_1}{\partial t} \right)^2 + \left(\frac{\partial u_2}{\partial t} \right)^2 + \left(\frac{\partial u_3}{\partial t} \right)^2 \right\} dx_1 \quad (2.17)$$

where ρ is material density and A is the sectional area.

Rotations

$$T_R = \frac{\rho}{2} \int_0^L \left\{ I_{x_2} \left(\frac{\partial \theta_2}{\partial t} \right)^2 + I_{x_3} \left(\frac{\partial \theta_3}{\partial t} \right)^2 \right\} dx_1 \quad (2.18)$$

Taking the symmetry of cross-section into consideration yields $I_{x_2} = I_{x_3} = I$. The Eq.

(2.18) becomes

$$T_R = \frac{\rho}{2} \int_0^L I \left[\left(\frac{\partial \theta_2}{\partial t} \right)^2 + \left(\frac{\partial \theta_3}{\partial t} \right)^2 \right] dx_1 \quad (2.19)$$

Torsion

$$T_\phi = \frac{\rho}{2} \int_0^L J \left(\frac{\partial \theta_1}{\partial t} \right)^2 dx_1 \quad (2.20)$$

where J is the polar area moment of inertia.

Utilizing the time derivative of Eq. (2.13), the total kinetic energy expression in term of the nodal displacement vector can be written as

$$T = T_R + T_T + T_\phi = \frac{1}{2} \{\dot{q}\}^T [M_e] \{\dot{q}\} \quad (2.21)$$

where $[M_e] = [M_T] + [M_R] + [M_\phi]$ is the augmented element mass matrix given by $[M_T]$ as the translational mass matrix, $[M_R]$ as the rotary inertia mass matrix and $[M_\phi]$ as the torsional mass matrix, defined by

$$[M_T] = \int_0^L [N_T]^T \rho A [N_T] dx_1 \quad (2.22)$$

$$[M_R] = \int_0^L [N_R]^T I [N_R] dx_1 \quad (2.23)$$

$$[M_\phi] = \int_0^L [N_\phi]^T J [N_\phi] dx_1 \quad (2.24)$$

2.3.3 Stiffness matrix

The elastic strain energy can be used to formulate element stiffness matrices. The strain energy per unit volume, U_0 , of the elastic body refers to the energy stored in the material and recovered as work when loading is removed; it is defined as

$$U_0 = \frac{1}{2} \{\sigma\}^T \{\varepsilon\} \quad (2.25)$$

For the linearly elastic material where the stress, σ , is related to the strain, ε , by $\{\sigma\} = [E]\{\varepsilon\}$ where E is the modulus of elasticity, Eq. (2.25) becomes

$$U_0 = \frac{1}{2} \{\varepsilon\}^T [E] \{\varepsilon\} \quad (2.26)$$

The total strain energy is written as

$$U = \int U_0 dV = \int \frac{1}{2} \{\sigma\}^T \{\varepsilon\} = \int \frac{1}{2} \{\varepsilon\}^T [E] \{\varepsilon\} dV \quad (2.27)$$

The elastic strain energy of axial, torsional, shear and bending deformations can be written in terms of the displacements as follows:

Axial deformation

$$U_A = \frac{1}{2} \int_0^L EA \left(\frac{\partial u_1}{\partial x_1} \right)^2 dx_1 \quad (2.28)$$

Torsional deformation

$$U_T = \frac{1}{2} \int_0^L GJ \left(\frac{\partial \theta_1}{\partial x_1} \right)^2 dx_1 \quad (2.29)$$

Shear deformation

$$U_S = \frac{1}{2} \int_0^L K_{S2} GA \left(\frac{\partial u_2}{\partial x_1} - \theta_3 \right)^2 dx_1 + \frac{1}{2} \int_0^L K_{S3} GA \left(\frac{\partial u_3}{\partial x_1} + \theta_2 \right)^2 dx_1 \quad (2.30)$$

Bending deformation

$$U_B = \frac{1}{2} \int_0^L EI_{x_2} \left(\frac{\partial \theta_2}{\partial x_1} \right)^2 dx_1 + \frac{1}{2} \int_0^L EI_{x_3} \left(\frac{\partial \theta_3}{\partial x_1} \right)^2 dx_1 \quad (2.31)$$

In addition, the beam stiffness also includes a stress stiffening term due to gravity, F_G , acting along the axis of the beam. The axial tensile load increases the lateral stiffness of the beam and provides a pendulum restoring torque. The stress stiffening strain energy is given by [27] as

$$U_G = \frac{1}{2} \int_0^L F_G(x_1) \left\{ \left(\frac{\partial u_2}{\partial x_1} \right)^2 + \left(\frac{\partial u_3}{\partial x_1} \right)^2 \right\} dx_1 \quad (2.32)$$

Thus, the total elastic strain energy becomes

$$U = U_A + U_T + U_S + U_B + U_G \quad (2.33)$$

Considering the symmetry of cross-section yields $K_{S2} = K_{S3} = K_S$ as well as $I_{x_2} = I_{x_3} = I$.

Equation (2.33) can be expressed as

$$\begin{aligned} U = & \frac{1}{2} \int_0^L EA \left(\frac{\partial u_1}{\partial x_1} \right)^2 dx_1 + \frac{1}{2} \int_0^L GJ \left(\frac{\partial \theta_1}{\partial x_1} \right)^2 dx_1 + \int_0^L \frac{K_S GA}{2} \left\{ \left(\frac{\partial u_2}{\partial x_1} - \theta_3 \right)^2 + \left(\frac{\partial u_3}{\partial x_1} + \theta_2 \right)^2 \right\} dx_1 \\ & + \int_0^L \frac{EI}{2} \left\{ \left(\frac{\partial \theta_2}{\partial x_1} \right)^2 + \left(\frac{\partial \theta_3}{\partial x_1} \right)^2 \right\} dx_1 + \int_0^L \frac{F_G(x_1)}{2} \left\{ \left(\frac{\partial u_2}{\partial x_1} \right)^2 + \left(\frac{\partial u_3}{\partial x_1} \right)^2 \right\} dx_1 \end{aligned} \quad (2.34)$$

Equation (2.34) can be written in matrix form as

$$U = \frac{1}{2} \{q\} [K_e] \{q\} \quad (2.35)$$

where $[K_e] = [K_A] + [K_T] + [K_S] + [K_B] + [K_G]$ is the augmented element stiffness matrix given by $[K_A]$ as the axial stiffness matrix, $[K_T]$ as the torsional stiffness matrix, $[K_S]$ as the shear stiffness matrix, $[K_B]$ as the bending stiffness matrix and $[K_G]$ as the stress stiffening matrix, defined by

$$[K_A] = \int_0^L EA \frac{\partial [N_{T_{u_1}}]}{\partial x_1} \frac{\partial [N_{T_{u_1}}]}{\partial x_1} dx_1 \quad (2.36)$$

$$[K_T] = \int_0^L GJ \frac{\partial [N_{R_{\theta_1}}]}{\partial x_1} \frac{\partial [N_{R_{\theta_1}}]}{\partial x_1} dx_1 \quad (2.37)$$

$$\begin{aligned}
[K_S] = \int_0^L \frac{K_S GA}{2} & \left\{ \left[\frac{\partial [N_{Tu_2}]}{\partial x_1} - [N_{R\theta_3}] \right]^T \left[\frac{\partial [N_{Tu_2}]}{\partial x_1} - [N_{R\theta_3}] \right] \right. \\
& \left. + \left[\frac{\partial [N_{Tu_3}]}{\partial x_1} - [N_{R\theta_2}] \right]^T \left[\frac{\partial [N_{Tu_3}]}{\partial x_1} - [N_{R\theta_2}] \right] \right\} dx_1 \quad (2.38)
\end{aligned}$$

$$[K_B] = \int_0^L \frac{EI}{2} \left\{ \frac{\partial [N_{R\theta_2}]}{\partial x_1} \frac{\partial [N_{R\theta_2}]}{\partial x_1} + \frac{\partial [N_{R\theta_3}]}{\partial x_1} \frac{\partial [N_{R\theta_3}]}{\partial x_1} \right\} dx_1 \quad (2.39)$$

$$[K_G] = \int_0^L \frac{F_G(x_1)}{2} \left\{ \frac{\partial [N_{Tu_2}]}{\partial x_1} \frac{\partial [N_{Tu_2}]}{\partial x_1} + \frac{\partial [N_{Tu_3}]}{\partial x_1} \frac{\partial [N_{Tu_3}]}{\partial x_1} \right\} dx_1 \quad (2.40)$$

2.3.4 Damping matrix

In this study, we used proportional damping, also known as Rayleigh damping, to represent viscous damping which is the energy dissipated in friction at drill collar connections and friction between the drill collar and other equipment. The global damping matrix $[C]$ is defined as a linear combination of the global mass matrix $[M]$ and global stiffness matrix $[K]$ [27].

$$[C] = \alpha[M] + \beta[K] \quad (2.41)$$

where α and β are proportional damping coefficients which have units of s^{-1} and s , respectively. The effect from $\alpha[M]$ damps lowest modes most heavily while the effect from $\beta[K]$ damps highest modes most heavily.

2.3.5 Equation of motion

Utilizing the standard finite element assembly procedure, we obtain the equation of motion in the assembled general form as

$$[M]\{\ddot{q}\} + [C]\{\dot{q}\} + [K]\{q\} = \{F\} \quad (2.42)$$

where $\{F\}$ is the force vector including the forces described in Section 2.2.

2.4 Modal approach

The modal approach uses fewer sets of degrees of freedom (DOF) to represent the full set of DOF in the finite element model. The described detail can be found in [27, 28].

We firstly solve the undamped free vibration equation of motion, Eq. (2.42)

$$[M]\{\ddot{q}\} + [K]\{q\} = \{0\} \quad (2.43)$$

to determine the eigenvalues λ_i which are equal to the square of the natural frequencies, ω_i , and their corresponding eigenvectors (or normal modes), $\{\phi\}_i$. By the orthogonality of the normal modes, we have

$$\{\phi\}_i^T [M] \{\phi\}_i = M_{ii} \quad , \quad \{\phi\}_i^T [K] \{\phi\}_i = K_{ii} \quad (2.44)$$

where M_{ii} and K_{ii} are the generalized mass and the generalized stiffness, respectively. If each $\{\phi\}_i$ is divided by the square root of M_{ii} , we obtain the orthonormal modes $\{\tilde{\phi}\}_i$. If N_m orthonormal modes are assembled as columns into a square matrix, that matrix is called the modal matrix $[\tilde{P}]$. The modal matrix can be used to decouple the equations of

motion. If we use the coordinate transformation $\{q\} = [\tilde{P}]\{y\}$ where $\{y\}$ is the modal coordinates and pre-multiply Eq. (2.42) by $[\tilde{P}]^T$, we obtain

$$\left([\tilde{P}]^T [M][\tilde{P}]\right)\{\ddot{y}\} + \left([\tilde{P}]^T [C][\tilde{P}]\right)\{\dot{y}\} + \left([\tilde{P}]^T [K][\tilde{P}]\right)\{y\} = [\tilde{P}]^T \{F\} \quad (2.45)$$

The $[\tilde{P}]^T [M][\tilde{P}]$ and $[\tilde{P}]^T [K][\tilde{P}]$ terms produce diagonal matrices

$$[\tilde{P}]^T [M][\tilde{P}] = [I], \quad [\tilde{P}]^T [K][\tilde{P}] = [\Lambda] \quad (2.46)$$

where $[I]$ is a unit matrix and $[\Lambda]$ is the diagonal matrix of the eigenvalues.

$$[\Lambda] = \begin{bmatrix} \lambda_1 & 0 & \cdots & 0 \\ 0 & \lambda_2 & \cdots & 0 \\ \vdots & \vdots & \ddots & \vdots \\ 0 & 0 & \cdots & \lambda_{N_m} \end{bmatrix} = \begin{bmatrix} \varpi_1^2 & 0 & \cdots & 0 \\ 0 & \varpi_2^2 & \cdots & 0 \\ \vdots & \vdots & \ddots & \vdots \\ 0 & 0 & \cdots & \varpi_{N_m}^2 \end{bmatrix} \quad (2.47)$$

Since we use proportional damping, $[\tilde{P}]^T [C][\tilde{P}]$ is diagonal as well and can be derived from Eq. (2.41).

$$\begin{aligned} [\tilde{P}]^T [C][\tilde{P}] &= \alpha [\tilde{P}]^T [M][\tilde{P}] + \beta [\tilde{P}]^T [K][\tilde{P}] \\ &= \alpha [I] + \beta [\Lambda] \end{aligned} \quad (2.48)$$

Thus Eq. (2.42) can be written as an uncoupled equation and its i th equation is in the form

$$\ddot{y}_i + 2\zeta_i \varpi_i \dot{y}_i + \varpi_i^2 y_i = \tilde{f}_i(t) \quad (2.49)$$

where \tilde{f}_i are the modal forces. The modal damping is defined as

$$2\zeta_i \varpi_i = \alpha + \beta \varpi_i^2 \quad (2.50)$$

where ζ_i are damping ratios and their typical value for structure is 2%. Since damping of higher modes is desired, therefore the value of α is set to be zero and β can be determined from Eq. (2.50).

The lowest modes in the modal matrix can represent the entire modes. Let N_r be the number of retained modes in modal matrix. The modal matrix $[\tilde{P}]$ becomes a $N_m \times N_r$ matrix and reduces the number of equations to be solved to N_r equations. We then solve for modal coordinates $\{y\}$ which is a $N_r \times 1$ matrix. The recovering of the physical coordinates $\{q\}$ can be made by the transformation equation

$$\{q\} = [\tilde{P}]\{y\} \quad (2.51)$$

2.5 Nonlinear dynamics techniques

The nonlinear dynamics techniques used in this work are

- 1) Lyapunov exponents
- 2) Bifurcation diagram
- 3) Poincaré map
- 4) Frequency spectrum

They are used to categorize the vibration behavior into harmonic, sub-harmonic, quasi-periodic or chaos. A harmonic response varies sinusoidally with time. If the driving frequency is ω , then a harmonic response has $2\pi/\omega$ -period and a sub-harmonic response has $2\pi n/\omega$ -period where n is an integer. If the response is the sum of two periodic functions and the ratio of the frequencies is not a rational number, the response is quasi-

periodic. The chaos is the non-periodic behavior and is apparently random or noisy [29, 30].

2.5.1 Lyapunov exponents

Detail regarding the calculation of Lyapunov exponents can be found in [29, 31, 32]. Lyapunov exponents are a measure of divergence or convergence of nearby trajectories. To calculate a Lyapunov exponent, we need to locate the initial points of two nearby trajectories in state space and follow the differences between these two trajectories. For a given nonlinear system, the set of n_e differential equations is represented by

$$\{\dot{x}\} = f(\{x\}) \quad (2.52)$$

The solution of the linearized form of Eq. (2.52) is denoted by $\{\eta\}$ and obtained from

$$\{\dot{\eta}\} = [A]\{\eta\} \quad (2.53)$$

where $[A] = [\nabla f]$ is $n_e \times n_e$ matrix of partial derivatives of f [29]. Equations (2.52) and (2.53) are simultaneously numerically integrated after the nonlinear system has reached steady state. Determining $\eta_i(t)$ for large t may lead to excess error on a computer due to exponential divergence along the chosen initial direction. Even though we expect to see the convergence from the initial direction, the numerical error occurring during integrating Eq. (2.52) directs the $\eta_i(t)$ along the exponentially diverged direction. To overcome these difficulties, we must carry out the integration over many time intervals with appropriate interval length (Δt) and form the new initial vectors before starting every new interval [29] as shown in Fig. 2.8.

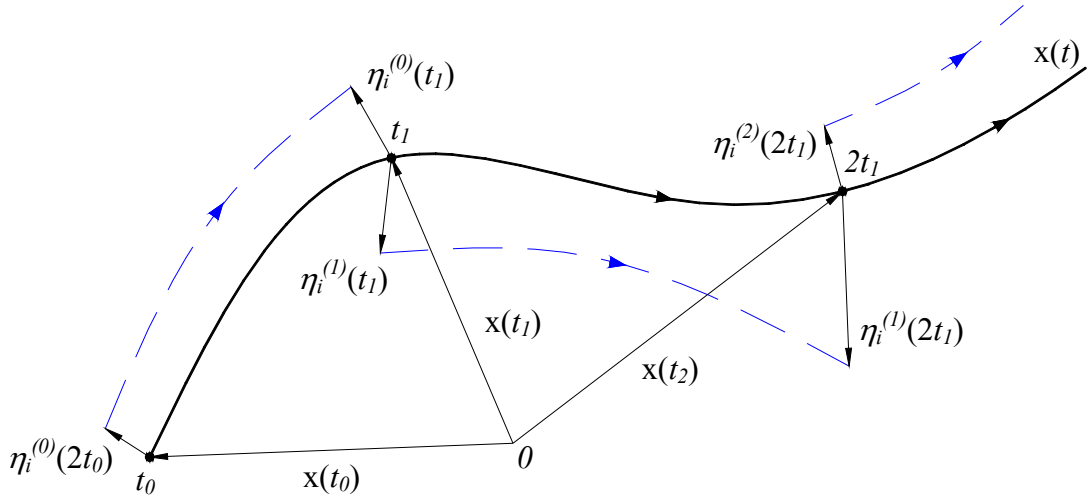


Figure 2.8. Sketch of the change in distance between two nearby trajectories [29].

A set of mutually orthonormal, initial condition vectors is calculated, using Gram-Schmidt orthogonalization, at the start of each time interval. Numerical integration of the linearized solution is started on each of these initial condition vectors and convergence or divergence of the resulting trajectories is evaluated. The first set of initial vectors at t_0 is:

$$\eta_1^{(0)}(t_0) = [1, 0, 0, \dots, 0], \eta_2^{(0)}(t_0) = [0, 1, 0, \dots, 0], \dots, \eta_n^{(0)}(t_0) = [0, 0, 0, \dots, 1] \quad (2.54)$$

The Gram-Schmidt procedure is then employed to construct a new set of orthonormal initial values after integrating over the interval $t_0 \leq t \leq t_1$. The Gram-Schmidt procedure is:

$$\eta_1^{(1)} = \eta_1^{(0)}(t_1),$$

$$\eta_2^{(1)} = \eta_2^{(0)}(t_1) - \frac{\eta_1^{(1)} \cdot \eta_2^{(0)}(t_1)}{\|\eta_1^{(1)}\|^2} \eta_1^{(1)},$$

through (2.55)

$$\eta_{n_e}^{(1)} = \eta_{n_e}^{(0)}(t_1) - \sum_{i=1}^{n_e-1} \frac{\eta_i^{(1)} \cdot \eta_{n_e}^{(0)}(t_1)}{\|\eta_i^{(1)}\|^2} \eta_i^{(1)}$$

where $(x \cdot y)$ denotes the inner product of the vectors x and y . The set of vectors

$\{\eta_1^{(1)}, \eta_2^{(1)}, \dots, \eta_{n_e}^{(1)}\}$ is orthogonal, and their orthonormal forms are given by

$$\hat{\eta}_1^{(1)} = \frac{\eta_1^{(1)}}{\|\eta_1^{(1)}\|}, \hat{\eta}_2^{(1)} = \frac{\eta_2^{(1)}}{\|\eta_2^{(1)}\|}, \dots, \hat{\eta}_n^{(1)} = \frac{\eta_n^{(1)}}{\|\eta_n^{(1)}\|} \quad (2.56)$$

The orthonormality can be verified by the following property:

$$\left(\left\{ \eta_1^{(k)}, \eta_2^{(k)}, \dots, \eta_{n_e}^{(k)} \right\}^T \cdot \left\{ \eta_1^{(k)}, \eta_2^{(k)}, \dots, \eta_{n_e}^{(k)} \right\} \right) = [I] \quad (2.57)$$

The norm in the denominator in Eq. (2.56) is denoted by N_i^k , where the superscript refers to the k th time interval and the subscript refers to the j th vector. The Lyapunov exponents are obtained after N_t time interval from

$$\lambda_i^{(N_t)} = \frac{1}{t_{N_t} - t_0} \sum_{k=1}^{N_t} \ln N_i^k \quad (2.58)$$

The norm N_i^k is the distance between the vectors $x(t_k) + \eta_i^{(k-1)}$ and $x(t_k)$. The distance exponentially grows in time for a chaotic system so that at least one of Lyapunov exponents will then be greater than zero ($\lambda > 0$). Therefore in this work the presence of chaos is indicated by a positive value of the maximum Lyapunov exponent. A computer flowchart for Lyapunov exponent calculation is shown in Fig. 2.9.

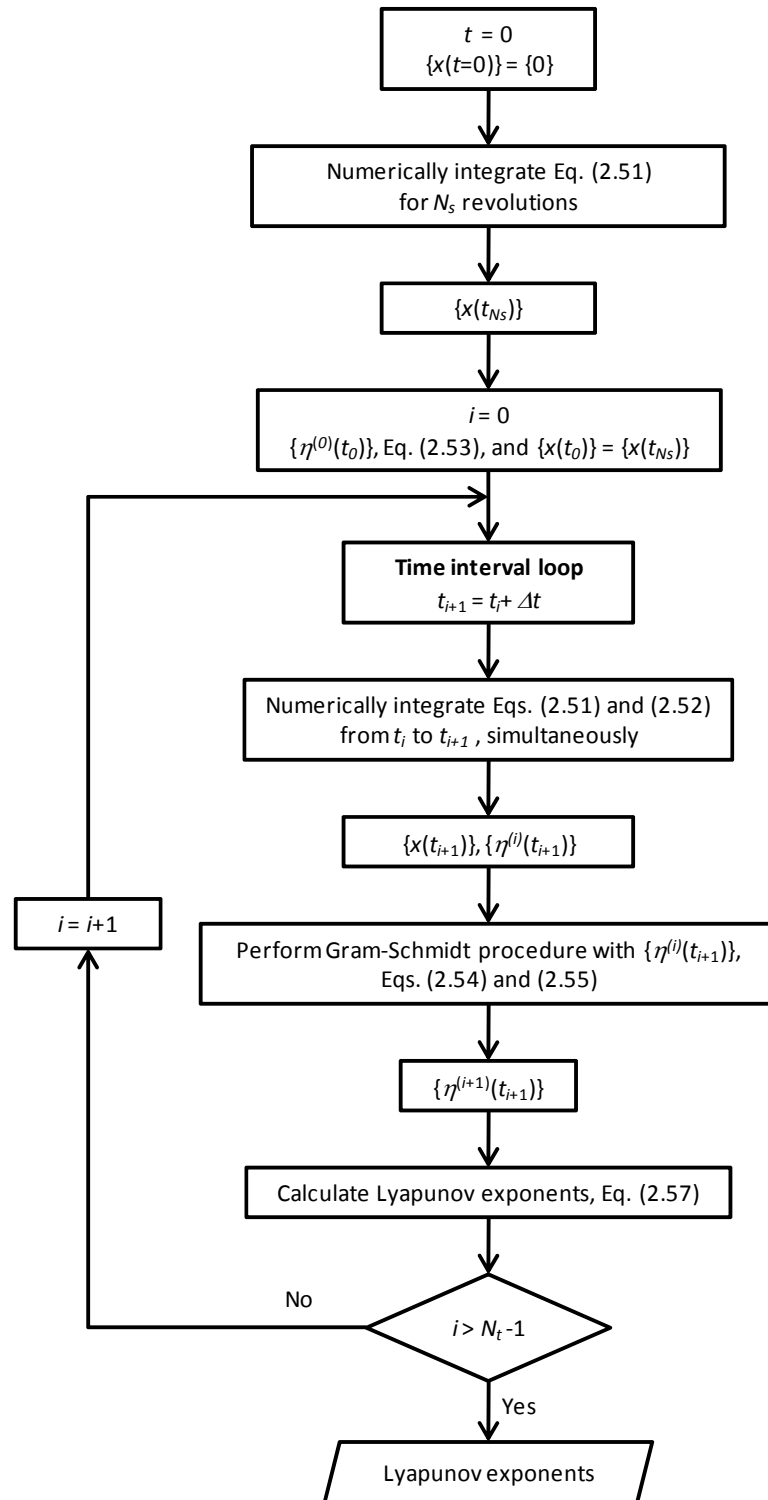


Figure 2.9. Computer flowchart for Lyapunov exponent calculation.

The accuracy of Lyapunov exponent prediction may be improved by the convergence study of the Lyapunov exponent factors including length of time to steady state (N_s), and the number (N_t) and duration (Δt) of time intervals.

2.5.2 Poincaré map

The Poincaré map refers to a sequence of points taken from the phase path at discrete times after steady state conditions have been attained [32, 33]. For example, if there is a driving force of period T , the Poincaré points are then taken along the phase path at time T , $2T$, $3T$, and so on. Therefore the phase plane, instead of showing a continuous line, will show the discrete points at intervals of the period T . When the motion is periodic, the Poincaré map on the phase plane appears as a finite set of points. For example, the Poincaré map corresponding to a period-1 harmonic appears a fixed point. If the motion is a period-2 sub-harmonic, the Poincaré map consists of a set of two points. For the quasi-periodic motion, the Poincaré points fill up a continuous closed curve. If the Poincaré map shows the area covered with points (strange attractor), the motion is defined as chaotic.

2.5.3 Bifurcation diagram

A bifurcation diagram [30, 33] is commonly used to examine the change in dynamical system behavior as the system parameter is varied. The characteristic value is plotted as the function of a system parameter after all the transients have died out. An abrupt change in the number of dots as the parameter varies indicates the occurrence of a

bifurcation such as period doubling, jump to another stable solution, etc. The bifurcation diagram shows a dot when the system parameter results in harmonic response. The finite set of dots appears on the part at which the system parameter results in sub-harmonic response. However when a line of dots at any system parameter exists, the response may be either quasi-periodic or chaotic.

2.5.4 Frequency spectrum

The distribution of frequency spectra is one of the principal approaches to distinguish the vibration response. By fast Fourier transform, the periodic or quasi-periodic motion will show a set of narrow spikes. If the motion is chaotic, a continuous distribution of frequencies will appear [32, 33].

Nonlinear response behavior is identified by employing one or more of these nonlinear dynamics techniques described above. Bifurcation diagrams are used to indicate the occurrence of a bifurcation as the parameter varies. Lyapunov exponents are a quantitative tool to indicate whether the response is chaotic or not. Poincaré map and frequency spectrum are used to confirm the characteristic of the response.

CHAPTER III

METHODOLOGY

According to the objectives of this work given in Chapter I, here we developed the methodology to achieve all objectives. The flowchart of proposed methodology is shown in Fig. 3.1 to provide better understanding of this work. The detail of each process will be discussed in this chapter.

3.1 Model

The model consists of a drill collar assembly and two stabilizers at its end points. The BHA is attached to the bottom of the drill collar in an actual drillstring. The BHA is much shorter and much lighter than the drill collar therefore we treat the BHA as an integral part of the drill collar in the model. The model parameters are partially adopted in [3, 10] and listed in Table 3.1. The model includes nonlinear damping, an imbalance force applied at the midspan location of the drill collar and linear damping at the stabilizers. The contact forces between the stabilizer and wellbore occur when the lateral displacement of the stabilizer becomes larger than the clearance (s_0). The drill collar mass is distributed uniformly along its entire length, which is an improvement over lumping the entire mass at the drill collar midspan as is done in reference [10, 11]. The drillstring is assumed to be uniform and made of linearly elastic, isotropic and homogeneous steel. The 2% damping ratio gives $\beta = 0.02$ and $\alpha = 0$ as described in

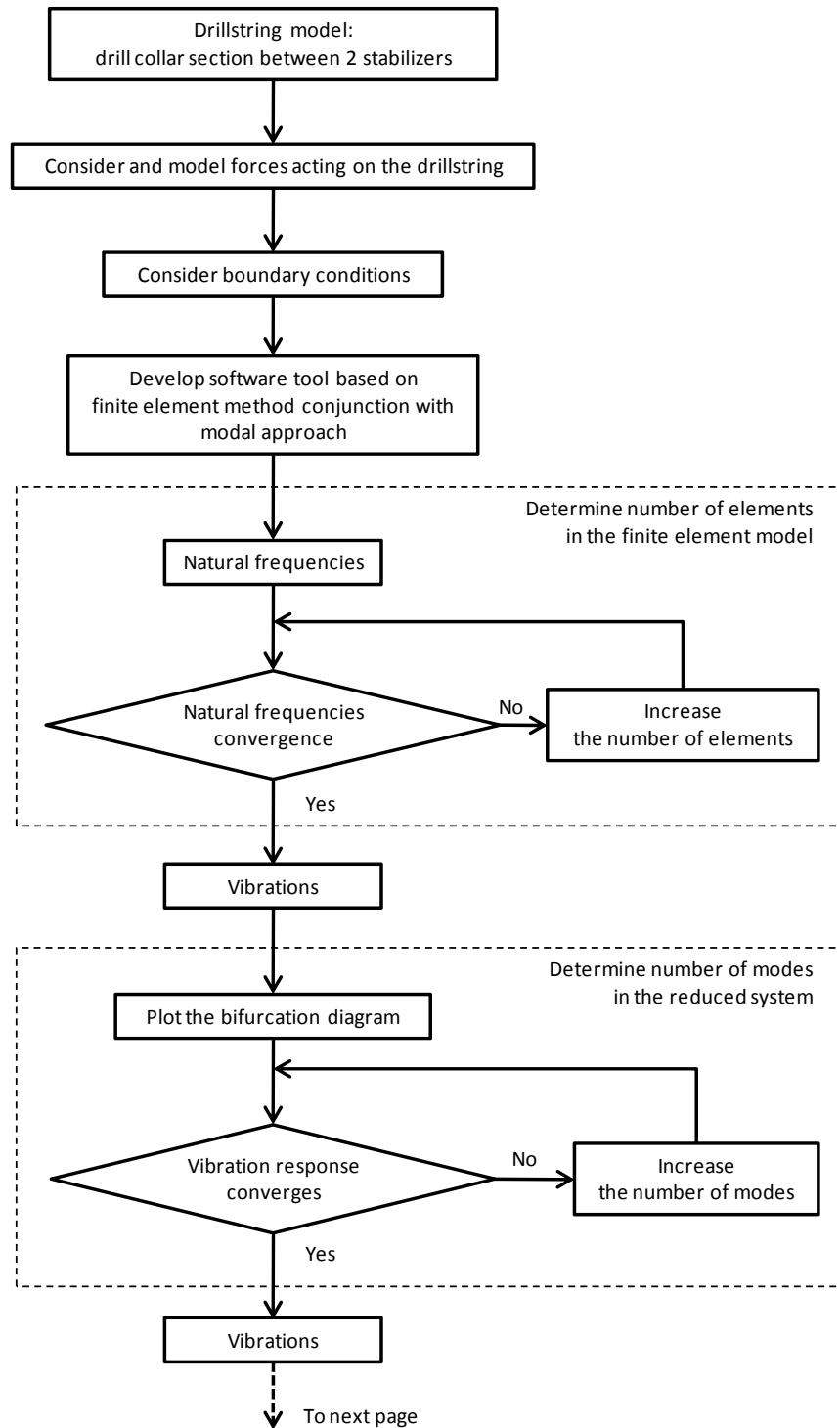


Figure 3.1. Flowchart of methodology in this work.

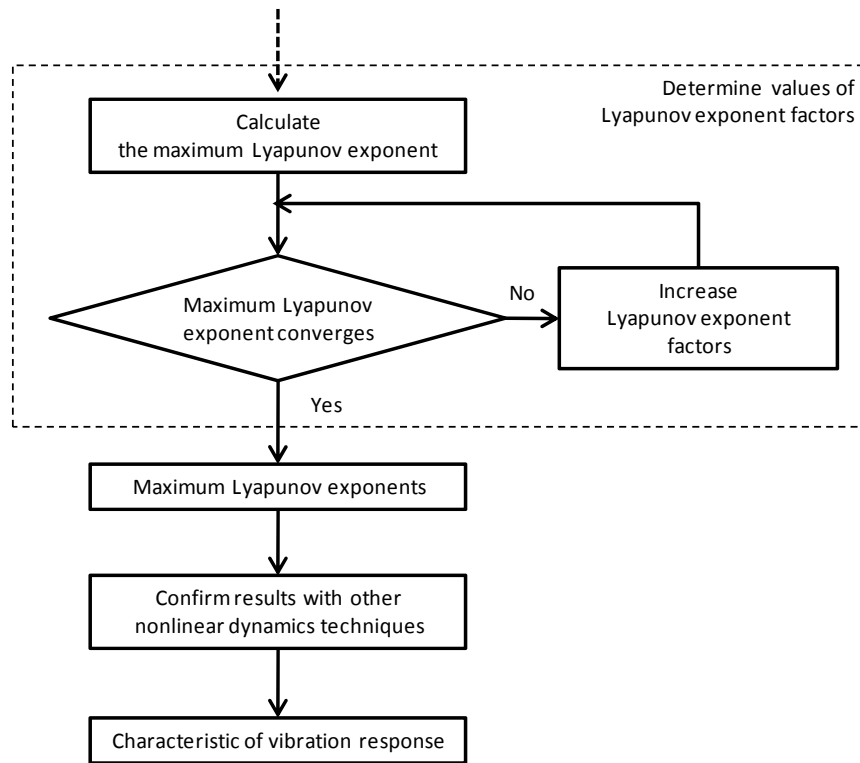


Figure 3.1. Flowchart of methodology in this work (continued).

Section 2.4. The model is assumed to have a constant rotational speed (rpm), Ω , which is valid under the assumption of uncoupled lateral and torsional motions. An imbalance force is positioned at the drill collar midspan in the model. The imbalance magnitude given in Table 3.1 is held constant for all results provided in this work. When the stabilizer contacts the wellbore, it is assumed to always slip along the wellbore.

Table 3.1. Parameters used in the simulations.

Drillpipe	
Drillpipe outside diameter	0.1016 m
Drillpipe inside diameter	0.0848 m
Drillpipe length ^a	100 m
Modulus of elasticity	2.1×10^{11} N/m ²
Material density, ρ	7850 kg/m ³
BHA (Drill collar)	
Drill collar outside diameter, D_c	0.2286 m
Drill collar inside diameter	0.0762 m
Drill collar length, L ^a	23 m
Modulus of elasticity	2.1×10^{11} N/m ²
Material density	7850 kg/m ³
Stabilizer clearance, s_0	0.0254 m
Drilling mud	
Drilling mud density, ρ_f	1500 kg/m ³
Drag coefficient, C_d	1
Imbalance force	
Drill collar mass, m_e	6587 kg
Mass eccentricity, e_0	0.0127 m
Contact force	
Wellbore stiffness, k_b ^a	1×10^8 N/m
Friction coefficient, μ_b ^a	0.2
Damping at stabilizers	
Damping coefficient, c_d ^a	300 N.s/m

^a Parameter values are assumed.

The boundary conditions of the drill collar–stabilizer model are free-free when the stabilizers are not in contact with the wellbore. This type of boundary condition was justified in reference [10] by the assumption that the spin (imbalance force) frequency is

near the lowest mode frequency of the isolated drill collar model as totally detached from the drillpipe above it. The assumption was validated in our work by simulating the model of the drill collar with and without the drillpipe attached. The drillpipe was assumed to be cantilevered at 100 meters above the top of the drill collar for this study shown in Fig. 3.2.

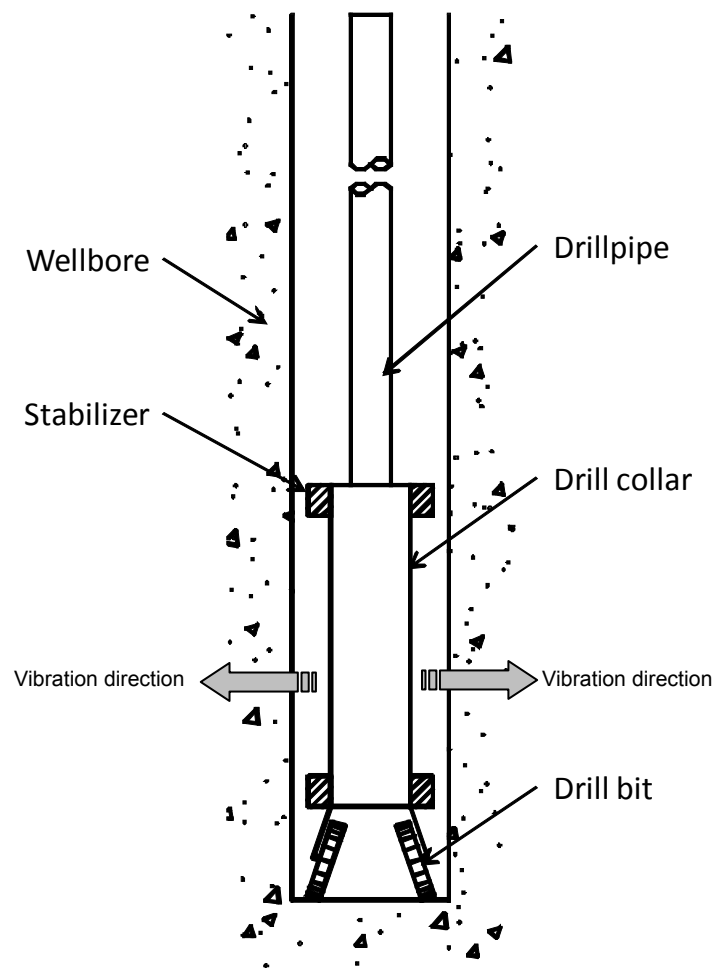


Figure 3.2. A general drillstring including the drillpipe, drill collar, stabilizers, and drill bit.

The ratio of the drill collar to drill pipe area moments of inertias was approximately 50 so that the drill collar is much stiffer than the drillpipe which also supports ignoring the drillpipe, by analogy to the “dog (drill collar) wagging the tail (drillpipe)”.

3.2 Finite element method conjunction with a modal method

The model described in Section 3.1 is divided into the Timoshenko beam finite elements consisting of two nodes at its ends as shown in Fig. 3.3. The model stiffness includes a stress stiffening effect due to drill collar weight acting along the axis of the drillstring. This axial tensile load increases the lateral stiffness of the drill string and provides a pendulum restoring torque. The stress stiffening strain energy is given by [27] as in Eq. (2.31). Inertia effects are modeled with a consistent mass matrix, including translational and rotary inertia terms. The system equation of motion is derived by using a Lagrangian approach. The kinetic energy is used to formulate element mass matrices and the elastic strain energy is used to formulate element stiffness matrices. The proportional damping is used to represent the viscous damping of the drillstring. The forces described in Chapter II which include imbalance, nonlinear and linear damping, and contact forces are treated as nodal forces. The model’s governing differential equations are numerically integrated with a Runge-Kutta algorithm including a variable time step to determine the lateral displacements and velocity.

The software tool is developed in Matlab to simulate vibrations and validated by comparing the lowest natural frequencies of each mode with the analytical solution given by Blevin [34]. The natural frequencies are obtained from the undamped system in

Eq. (2.42). Although the accuracy of the solution from the finite element model increases as the number of elements increases, the computational time also increases. The number of elements (N_e) is determined by the convergence study of the lowest natural frequencies.

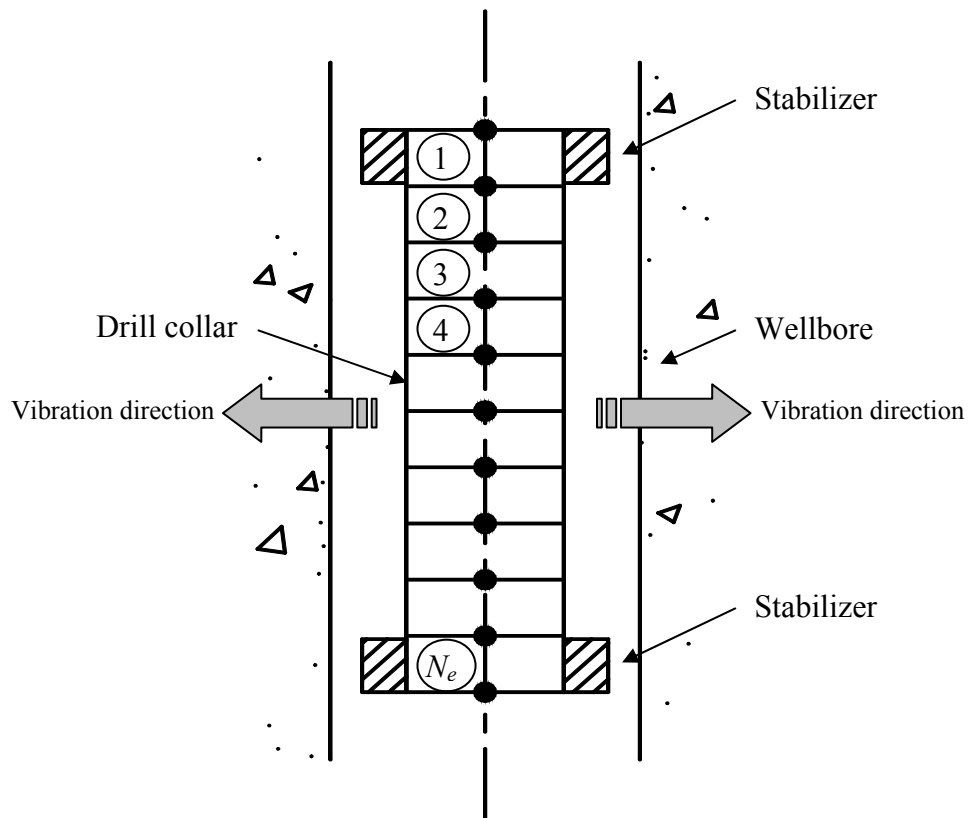


Figure 3.3. The finite element model.

The direct integration of the system equation of motion is computation time prohibitive because of the large number of degrees of freedom and the presence of nonlinear forces that require very small integration time steps. Therefore a modal condensation method is then utilized to reduce the number of degrees of freedom in the

finite element system and computation time. This requires selection of the number and types of modes used in the reduced system. The convergence study of the response behavior on the bifurcation diagram is then conducted.

3.3 Nonlinear dynamics analysis

Nonlinear response behavior is identified by employing one or more of the following nonlinear dynamics techniques: Lyapunov exponents, Poincaré maps, bifurcation diagrams and frequency spectrum. The bifurcation diagram is used to indicate a bifurcation as the parameter varies. For a chaotic system, at least one of Lyapunov exponents becomes positive. Therefore the presence of the chaos is indicated by a positive value of the maximum Lyapunov exponent. The Poincaré map and frequency spectrum are then used to confirm the results.

The Gram-Schmidt procedure used in the Lyapunov exponent calculation is validated by an orthonormality test given in Eq. (2.56). Moreover, Lyapunov exponents depend on the length of time to steady state, the number of time intervals that are utilized and the length of these time intervals. The values of these three factors have to be determined by convergence studies before being brought into the calculation.

3.4 Study cases

In this work we study the effects of nonlinear forces on the chaotic vibrations. Three sources of nonlinear sources in the model are

- a) a quadratic damper due to surrounding mudflow,

- b) the intermittent contact forces between the stabilizers and wellbore, and
- c) the friction force between the stabilizer and wellbore.

Also the effects of physical parameters including the friction coefficient (μ_b), drill collar length (L), and clearance between the stabilizer and wellbore (s_0) are studied as follow:

- a) Friction coefficient is varied from 0.1, 0.2 and 0.3.
- b) Drill collar length is varied from 15 to 25 meters.
- c) Stabilizer clearance is varied from 0.0127, 0.0254 and 0.0508 meters.

CHAPTER IV

RESULTS

In this chapter, all results of this work are shown. The convergence studies to determine the number of elements in the finite element system, the number of modes in the reduced system and the values of the Lyapunov exponent factors are shown in Section 4.1. The assumption of the boundary condition and the developed program are validated in Section 4.2. Lastly, Section 4.3 shows vibration behavior which is obtained from varying system parameters and characterized by the use of nonlinear dynamics techniques.

4.1 Convergence studies

Convergence studies in this work are as follow:

- a) the number of elements used in the finite element system,
- b) the number of modes in the reduced system,
- c) the values of the Lyapunov exponent factors: the length of time to steady state, the number of time intervals, and the length of time interval used in the Lyapunov exponent calculation

We determine the number of elements used in the finite element system by the study of the natural frequency convergence. The first ten natural frequencies obtained from varying numbers of elements in the finite element system from 4, 6, 8, 10, 12 and 14 are

shown in Table 4.1. The natural frequencies start converging after using 10 elements. Therefore, we utilize 10 finite elements for all results provided in this work.

The simulation times are considered excessive to employ physical coordinates for this work. Thus modal method is utilized to reduce the number of degrees of freedom in the system and the computational time. The number of modes used in the reduced system is determined by the convergence study of vibration behavior shown on bifurcation diagrams.

Table 4.1. The first ten natural frequencies of the model.

Natural frequencies	Number of elements					
	4	6	8	10	12	14
1	0	0	0	0	0	0
2	0.2822	0.2723	0.2674	0.2643	0.2622	0.2608
3	2.1770	2.1700	2.1670	2.1654	2.1643	2.1635
4	5.8763	5.8453	5.8365	5.8332	5.8315	5.8306
5	11.4601	11.4328	11.3887	11.3734	11.367	11.3638
6	20.9578	18.9733	18.8323	18.7737	18.749	18.7373
7	32.7622	28.2461	28.2262	28.0619	27.9876	27.9515
8	35.0903	34.9655	34.9219	34.9017	34.8908	34.8841
9	50.7697	43.3185	39.6099	39.2875	39.1063	39.0149
10	56.5814	56.3502	52.4243	52.5086	52.1465	51.9479

Figure 4.1 shows the convergence of vibration behavior on bifurcation diagrams when using 8, 9, 10 and 11 modes. Both rigid body and flexible modes are included in order to

produce both types of behavior in the system response. The bifurcation diagram plots the instantaneous transverse velocity (v_{x2}) at the drill collar midspan location at the starting time for each revolution versus rpm (spin rate). Table 4.2 shows the chaos onset speed at which the plot bifurcates from a harmonic response (single dot) to a chaotic response when the number of modes is varied from 8 to 12. The bifurcation diagrams are found to converge with 10 modes and the chaos onset speed is 51.6 rpm.

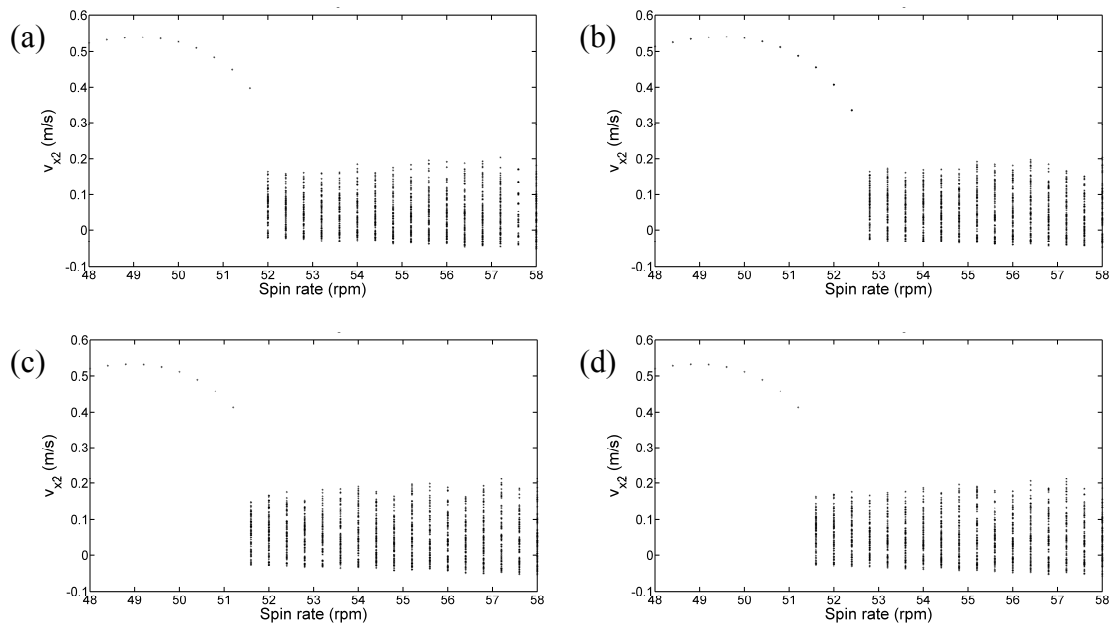


Figure 4.1. Bifurcation diagrams when using different numbers of modes

(a) 8 modes (b) 9 modes (c) 10 modes and (d) 11 modes.

Figure 4.2 shows the displacement response (x_2) at the center of drill collar and at one of the stabilizers obtained from full system and reduced system at 40 rpm. The response is

sinusoidal at this rpm. Figure 4.3 shows chaotic responses at 55 rpm. The response locations in Fig. 4.3 are the same as in Fig. 4.2. These figures show almost no difference between the vibration responses obtained from full and reduced systems for both a chaotic rpm and a non-chaotic rpm. Therefore, the reduced system can represent the full system and reduce the computational time. In this work we then utilize 10 modes for all simulations.

Table 4.2. The chaos onset speed when varying number of modes.

Number of modes	Chaos onset speed (rpm)
8	52.8
9	52
10	51.6
11	51.6
12	51.6

The values of Lyapunov exponent factors have to be determined before being used in the calculation. Tables 4.3, 4.4 and 4.5 show the dependence and convergence properties of the maximum Lyapunov exponents on the three factors described in Chapter II for a chaotic response (55 rpm). The model parameters in this case are:

$$L = 23\text{m}, \mu_b = 0.1, s_0 = 2.54 \text{ cm.}$$

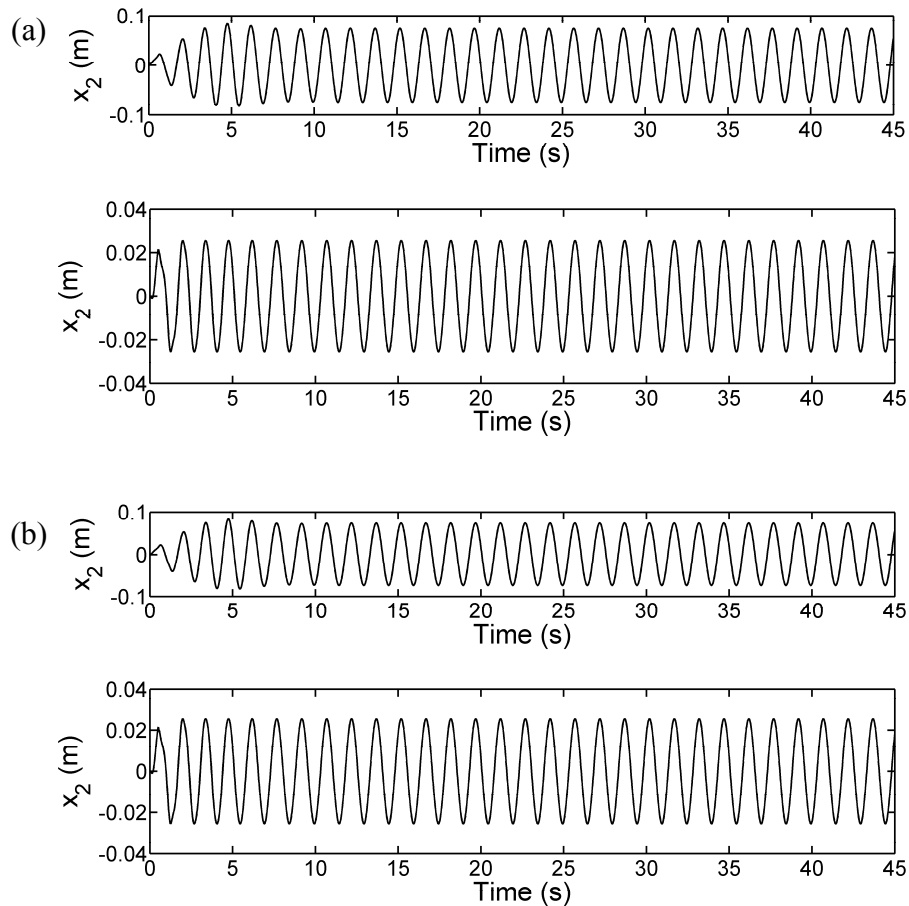


Figure 4.2. Vibrations at drill collar center (top) and stabilizer (bottom) obtained from (a) full system and (b) reduced system for a non-chaotic response.

Table 4.3 utilized 200 time intervals with 0.1 revolutions per interval. Table 4.4 utilized 2000 revolutions as a time to steady state and 0.1 revolutions per time interval. Table 4.5 utilized 2000 revolutions to steady state and 500 time intervals. It can be concluded from these tables that the accurate Lyapunov exponents require approximately 2000 revolutions to reach steady state and 500 time intervals with 0.1 revolutions per interval.

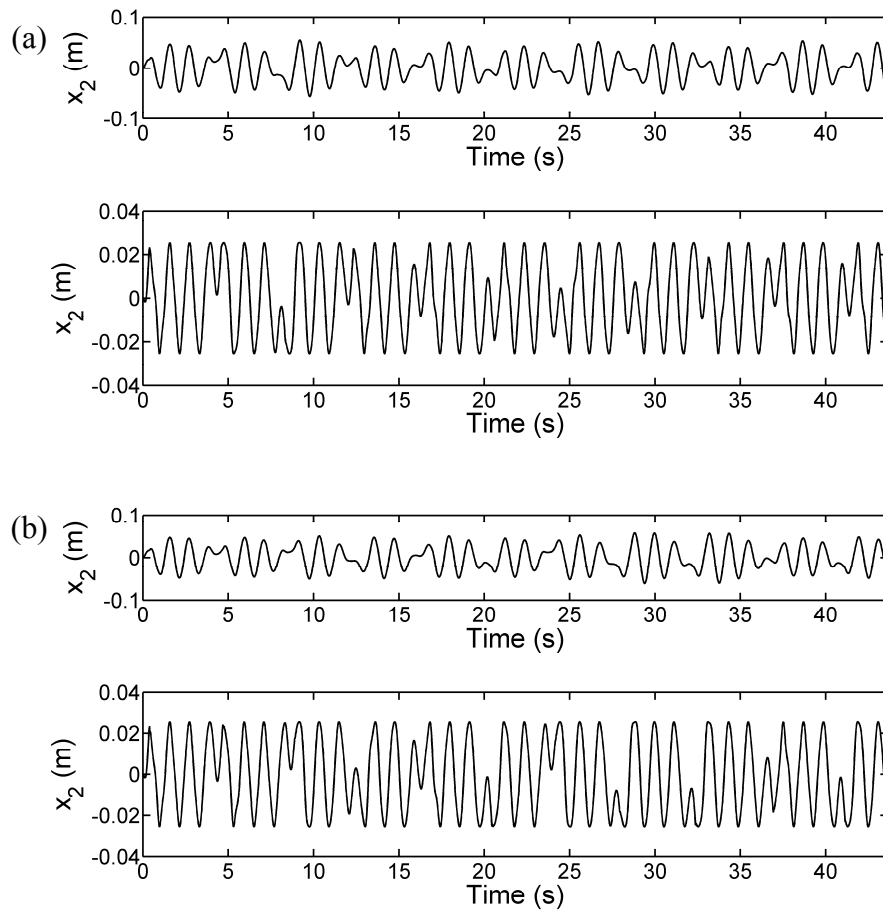


Figure 4.3. Vibrations at drill collar center (top) and stabilizer (bottom) obtained from (a) full system and (b) reduced system for a chaotic response.

Figures 4.4(a) and (b) show how the maximum Lyapunov exponent converges with time for both a non-chaotic (45 rpm) and a chaotic (55 rpm) response, respectively. The Lyapunov exponents are determined for the same conditions as for Table 4.3, 4.4 and 4.5. The maximum Lyapunov exponent converges to a negative value for a non-chaotic response and converges to a positive value for a chaotic response.

Table 4.3. Maximum Lyapunov exponents for different times to steady state.

Time to steady state (rev)	Maximum Lyapunov exponent
50	0.3897
100	0.4714
500	0.3314
1000	0.5108
1500	0.1710
2000	0.1892
2500	0.1403
3000	0.2515
3500	0.2601
4000	0.2204
4500	0.2083
5000	0.1690

Table 4.4. Maximum Lyapunov exponents obtained from different numbers of time intervals.

Number of time intervals	Maximum Lyapunov exponent
50	0.5178
100	0.2225
200	0.1892
500	0.1157
700	0.0962
1000	0.1008
1500	0.0933
2000	0.0844

Table 4.5. Maximum Lyapunov exponents obtained from varying the time interval duration.

Length of time interval	Maximum Lyapunov exponent
0.01 *rev	0.5178
0.05 *rev	0.1746
0.10 *rev	0.1157
0.20 *rev	0.1005

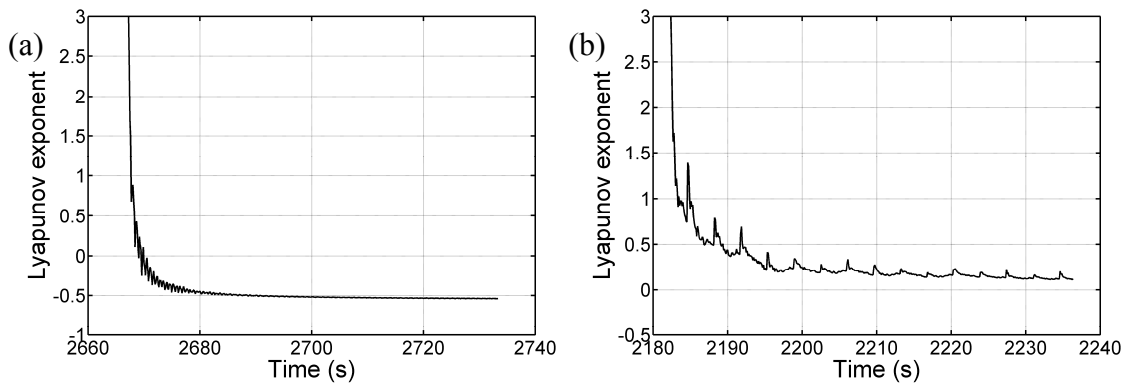


Figure 4.4. Maximum Lyapunov exponent convergence with time for (a) a non-chaotic and (b) a chaotic response.

The rigid body modes have the effect on the accuracy of the Lyapunov exponent prediction of chaos. If the top of the drill collar is not fixed for axial and torsional vibrations, the obtained rigid body modes with zero natural frequency are for coupled axial, torsional and lateral modes. With this boundary condition, maximum Lyapunov

exponents for a non-chaotic rpm are greater than zero which is an incorrect prediction. Constraining axial and torsional motions at the top of drill collar can solve this problem and give the rigid body modes for pure translation. This assumption is valid for the lateral model.

4.2 Model validation

4.2.1 Boundary condition

The assumption that the spin frequency is near the lowest mode frequency of the isolated drill collar model as totally detached from the drillpipe above it is validated here. The five lowest free-free natural frequencies and mode shapes are shown in Table 4.6 and Fig. 4.5 respectively. The results are obtained from the model without drillpipe.

Table 4.6. Free–free natural frequencies of drill collar-stabilizer model.

Mode	Natural frequencies (Hz)	Damping ratio
1	0	-
2	0.2643	0.0166
3	2.1654	0.1361
4	5.8332	0.3665
5	11.3734	0.7146

From Fig. 4.5, the 1st rigid body mode is for pure translation. The second rigid body mode has a slightly positive, non-zero value due to the gravity (pendulum)

restoring torque (Eq. 2.32) on the rotational mode. These are some of the modes utilized in the modal response simulations.

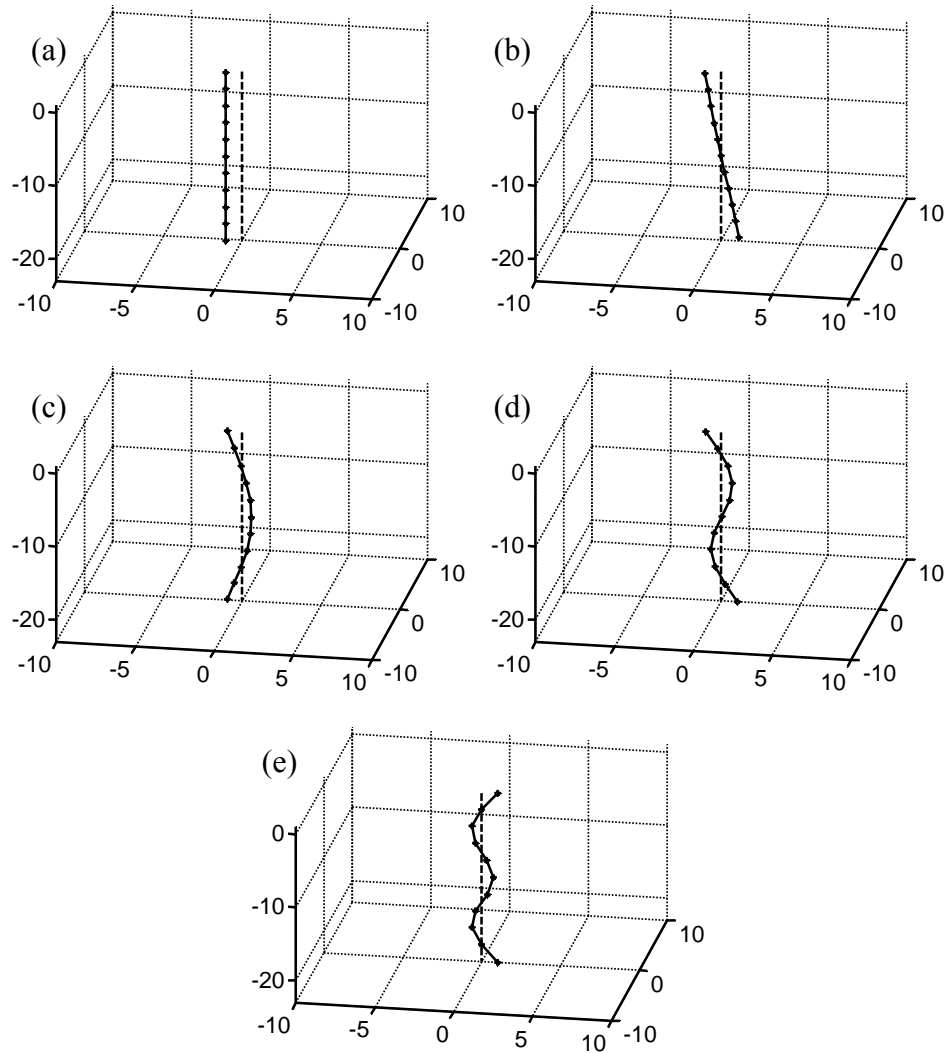


Figure 4.5. Five lowest mode shapes of the drill collar–stabilizer model

(a) mode 1 (b) mode 2 (c) mode 3 (d) mode 4 (e) mode 5.

Figure 4.6 shows the displacement response at the center of the drill collar and at one of the stabilizers for the “with” and “without” drillpipe cases, at 40 rpm. The response is seen to be sinusoidal at this rpm. Figure 4.7 shows the same responses at 55 rpm, at which the response is chaotic. The response locations are the same as for Fig. 4.6.

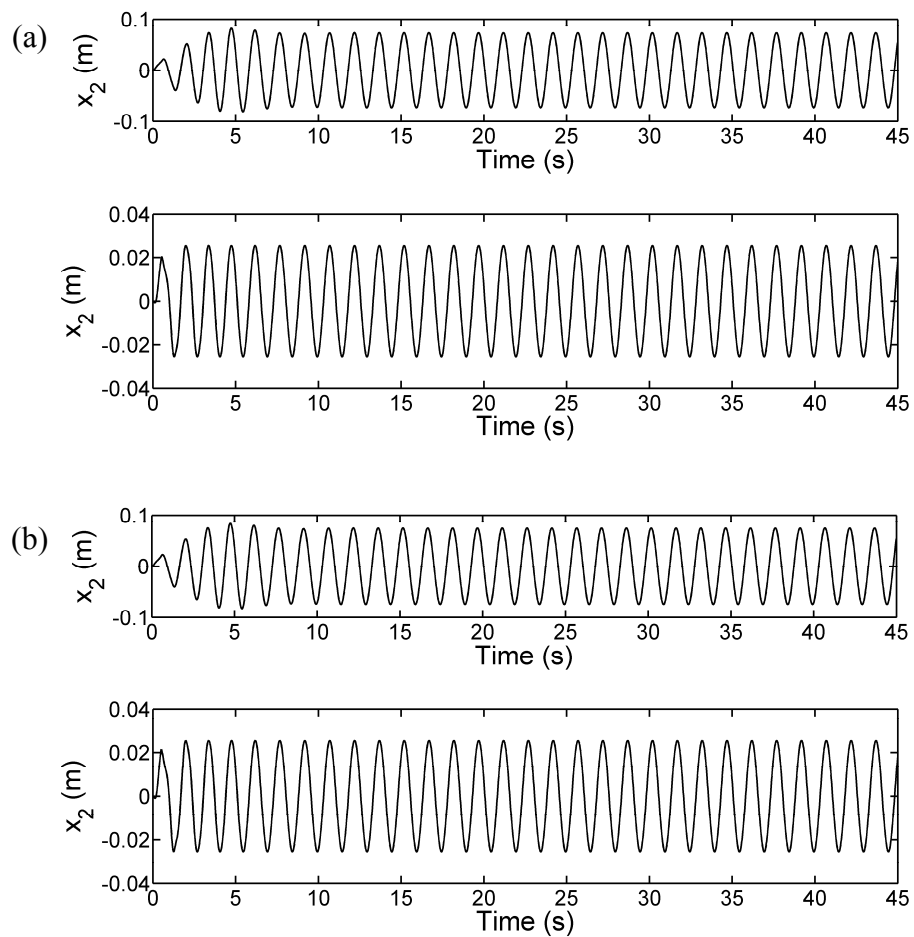


Figure 4.6. Vibrations at the drill collar center (top) and stabilizer (bottom), with (a) and without (b) the drillpipe, for a non-chaotic rpm.

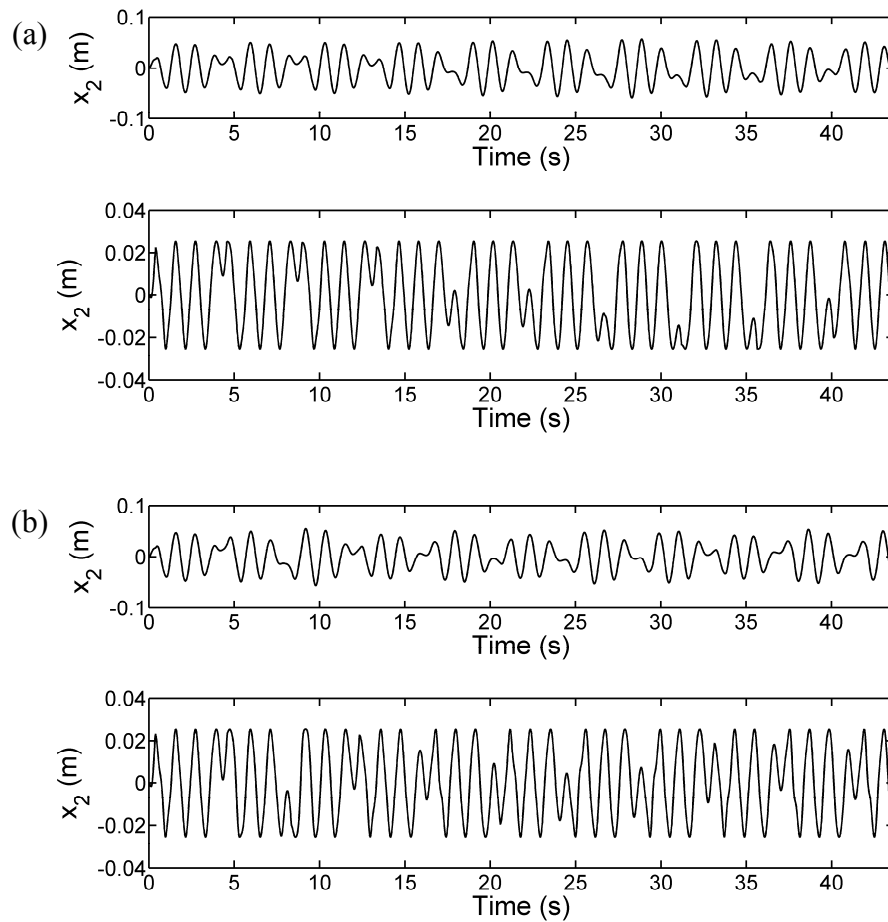


Figure 4.7. Vibrations at the drill collar center (top) and stabilizer (bottom), with (a) and without (b) the drillpipe, for a chaotic rpm.

Figures 4.6 and 4.7 clearly show almost no difference with and without the drillpipe, which supports its removal from the model from all of the remaining simulations. The bottom free boundary condition on the drill collar is most appropriate with light weight on bit (WOB) operation. A lateral degree of freedom is assumed at the bit. This is a reasonable assumption because of oversize cutting (bit walk, runout, and formation swell

compensation) which leaves a clearance between the bit-through diameter and the as drilled gage hole.

4.2.2 Software tool

Table 4.7 shows the lowest natural frequencies of axial, torsional and lateral vibrations obtained from the analytical solution given by [34] and the developed software. The table shows slight difference between natural frequencies from these two methods. The difference is less than 5%.

Table 4.7. The lowest natural frequencies obtained from the analytical solution and the developed software.

Vibration modes	Analytical solution	Software
Axial	56.219	56.568
Torsional	34.869	34.902
Lateral	2.097	2.097

The Gram-Schmidt procedure is validated by an orthogonality test. The maximum off-diagonal terms in the identity matrix obtained from Eq. (2.57) at each time interval are shown in Fig. 4.8. The conditions in this case are the same as in Fig. 4.4 for both chaotic and non-chaotic rpm. The maximum off-diagonal terms are very small hence they are considered as zeros.

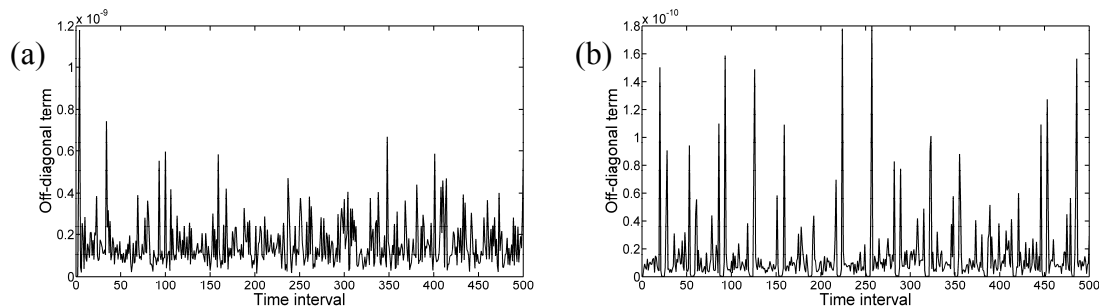


Figure 4.8. Maximum off-diagonal term in the identity matrix versus time interval for (a) a non-chaotic rpm and (b) a chaotic rpm.

4.3 The effects of the system parameters on the vibration behavior

4.3.1 Nonlinear forces

There are three sources of nonlinear forces in the model, including

- a) a quadratic damper applied at the center of the drillstring to model the interaction force between the vibrating drill collar and the surrounding mud flow,
- b) the intermittent contact forces between the stabilizers and the wellbore, and
- c) the friction force between the stabilizers and the wellbore

Each of the nonlinear forces discussed above have an influence on the predicted chaotic vibrations. To illustrate this consider the next four figures which correspond to a model that has intermittent contact between the drill collar stabilizers and wellbore. Figure 4.9(a) shows a bifurcation diagram for the model with no quadratic damping and no friction. The plot bifurcates from a harmonic response (single dot) to a chaotic response at 55.2 rpm. Figure 4.9(b) shows a bifurcation diagram for the model with quadratic damping and no friction. The plot bifurcates from a harmonic response to a chaotic

response at 52.8 rpm. Figure 4.9(c) shows a bifurcation diagram for the model without quadratic damping and with friction. The plot bifurcates from a harmonic response to a chaotic response at 52.4 rpm. Figure 4.9(d) shows a bifurcation diagram for the model with quadratic damping and with friction. The plot bifurcates from a harmonic response to a chaotic response at 49.6 rpm. These diagrams plot the transverse velocity at the drill collar midspan location versus rpm. Clearly these figures confirm that each type of nonlinear force has an influence on the nonlinear dynamic behavior of the systems based on the changes in chaos onset speed. Figure 4.8(a) shows that the clearance between the stabilizer and wellbore in this case ($s_0 = 2.54$ cm) is sufficient to cause bifurcation and chaos.

4.3.2 Physical parameter effects

The effects of the following physical parameters on the chaos are studied.

- a) The coefficient of friction at the wellbore (μ_b)
- b) Drill collar length (L)
- c) Clearance between the stabilizer and wellbore (s_0)

Figure 4.10 shows that the chaos onset rpm and response amplitudes decrease as the coefficient of friction increases from 0.1 to 0.3. This diagram contains the transverse motion velocity at the drill collar midspan location. The maximum Lyapunov exponent was determined for the same conditions as in Fig. 4.10 and is shown plotted against rpm in Fig. 4.11. The zero crossings in these plots clearly confirm the transition between

harmonic and chaotic response as implied in Fig. 4.10. For sake of reference the Lyapunov exponents are determined after 2000 revolutions to insure steady state conditions. The number and duration of the time intervals for evaluating the Lyapunov exponents are 500 and 0.1 revolution per period, respectively.

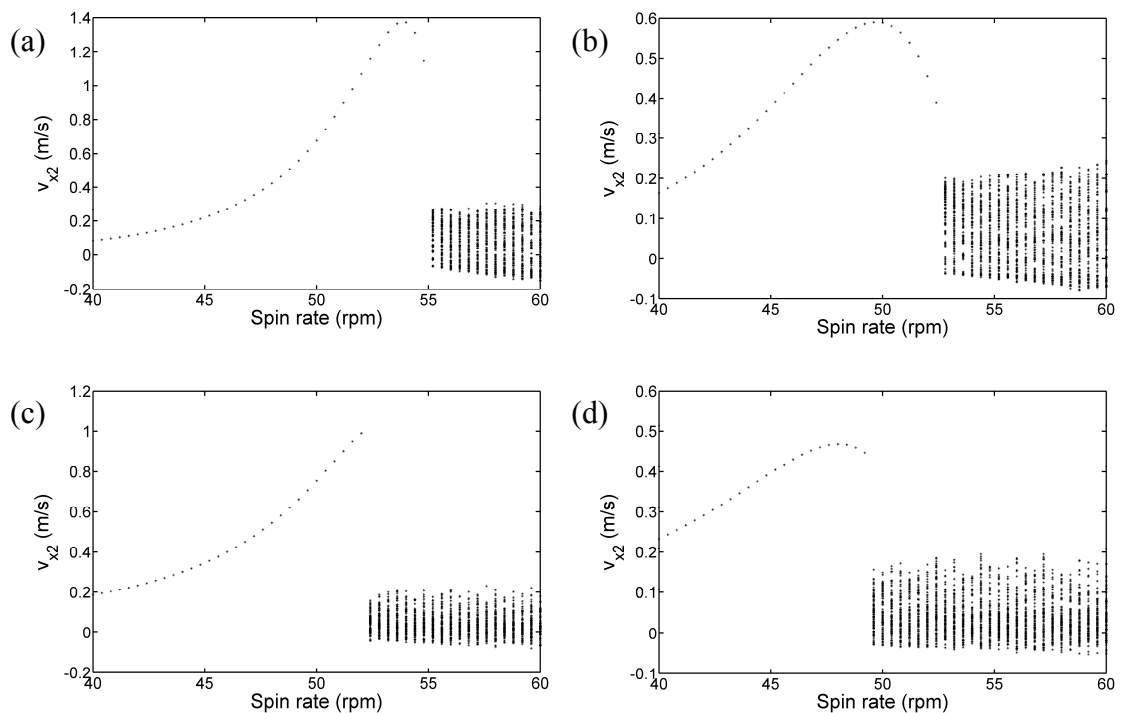


Figure 4.9. Bifurcation diagrams showing the influence of nonlinear forces on chaotic vibrations (a) without friction and quadratic damping (b) without friction and with quadratic damping (c) with friction and without quadratic damping and (d) with friction and with quadratic damping.

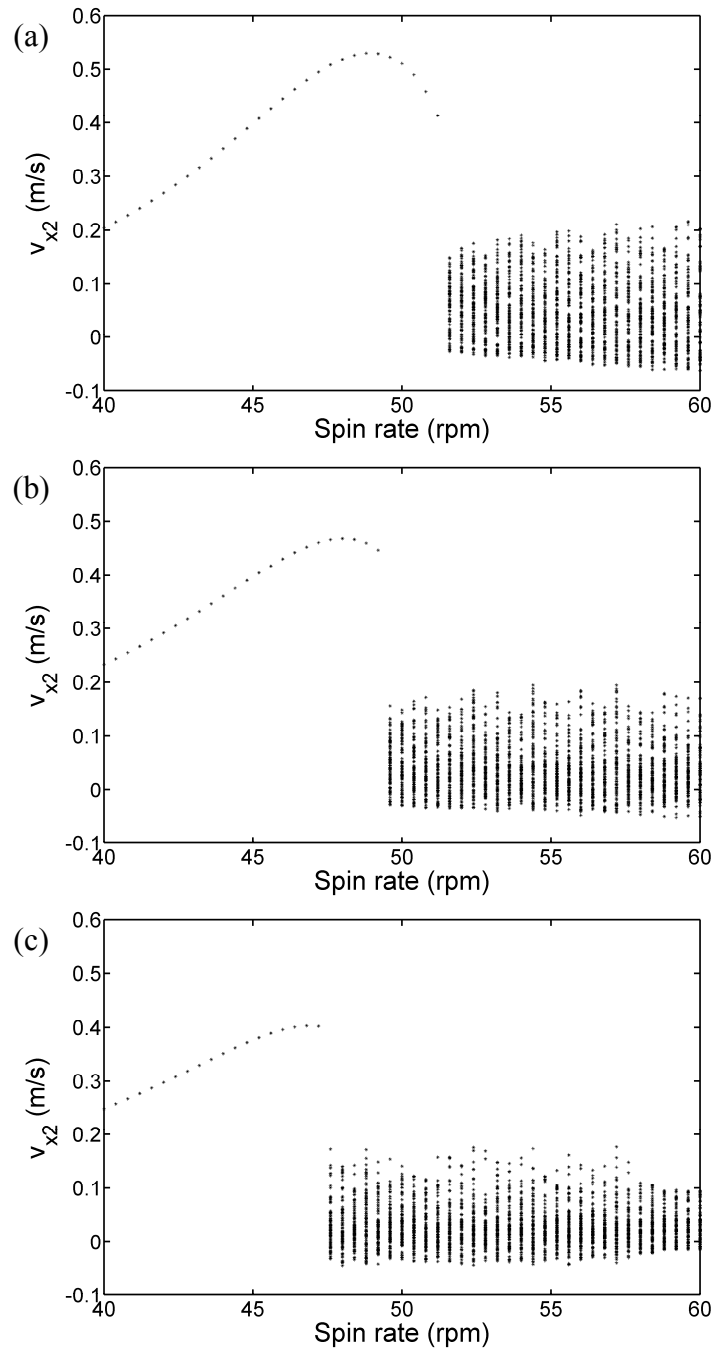


Figure 4.10. Bifurcation diagrams for model with different coefficients of friction

(a) $\mu_b = 0.1$ (b) $\mu_b = 0.2$ and (c) $\mu_b = 0.3$.

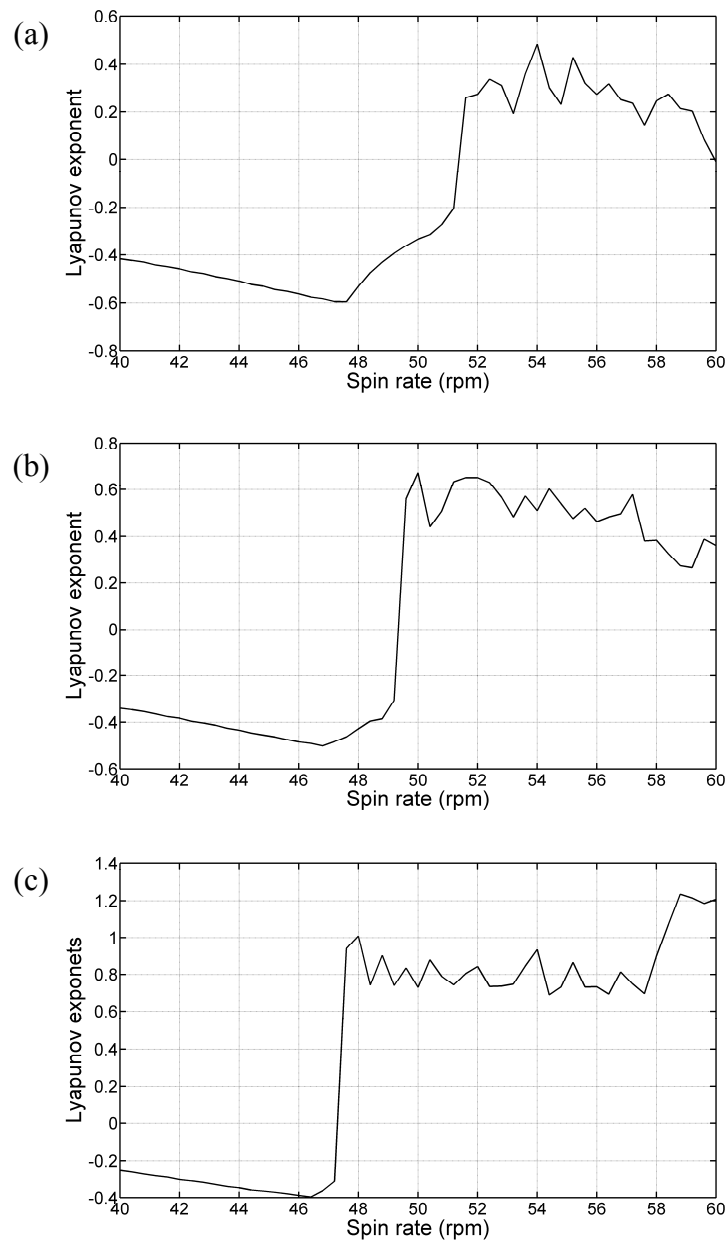


Figure 4.11. Maximum Lyapunov exponent versus drillstring rpm with different coefficients of friction (a) $\mu_b = 0.1$ (b) $\mu_b = 0.2$ and (c) $\mu_b = 0.3$.

Table 4.8 and Fig. 4.12 show the effect of changing the drill collar length on the bifurcation diagram parameters and the chaos onset speed, respectively. The peak vibration amplitude and chaos onset speed are seen to decrease as the drill collar length increases from 15, 20, 21, 22, 23 and 25 meters.

Table 4.8. The chaos onset speed when varying the length of the drill collar.

Length of drill collar (m)	Chaos onset speed (rpm)
15	108.4
20	64
21	58.4
22	53.6
23	49.6
25	42.4

Figure 4.13 shows the bifurcation diagram for the drill collar midspan, transverse velocity with the stabilizer clearance varied from 0.0127, 0.0254 and 0.0508 meters. These results indicate that clearance has a significant effect on the presence of chaos. The absence of chaos for the smallest clearance indicates that a decrease in clearance may mitigate chaos. Figure 4.14 shows the maximum Lyapunov exponent determined for the same conditions as in Fig. 4.13 and plotted against rpm.

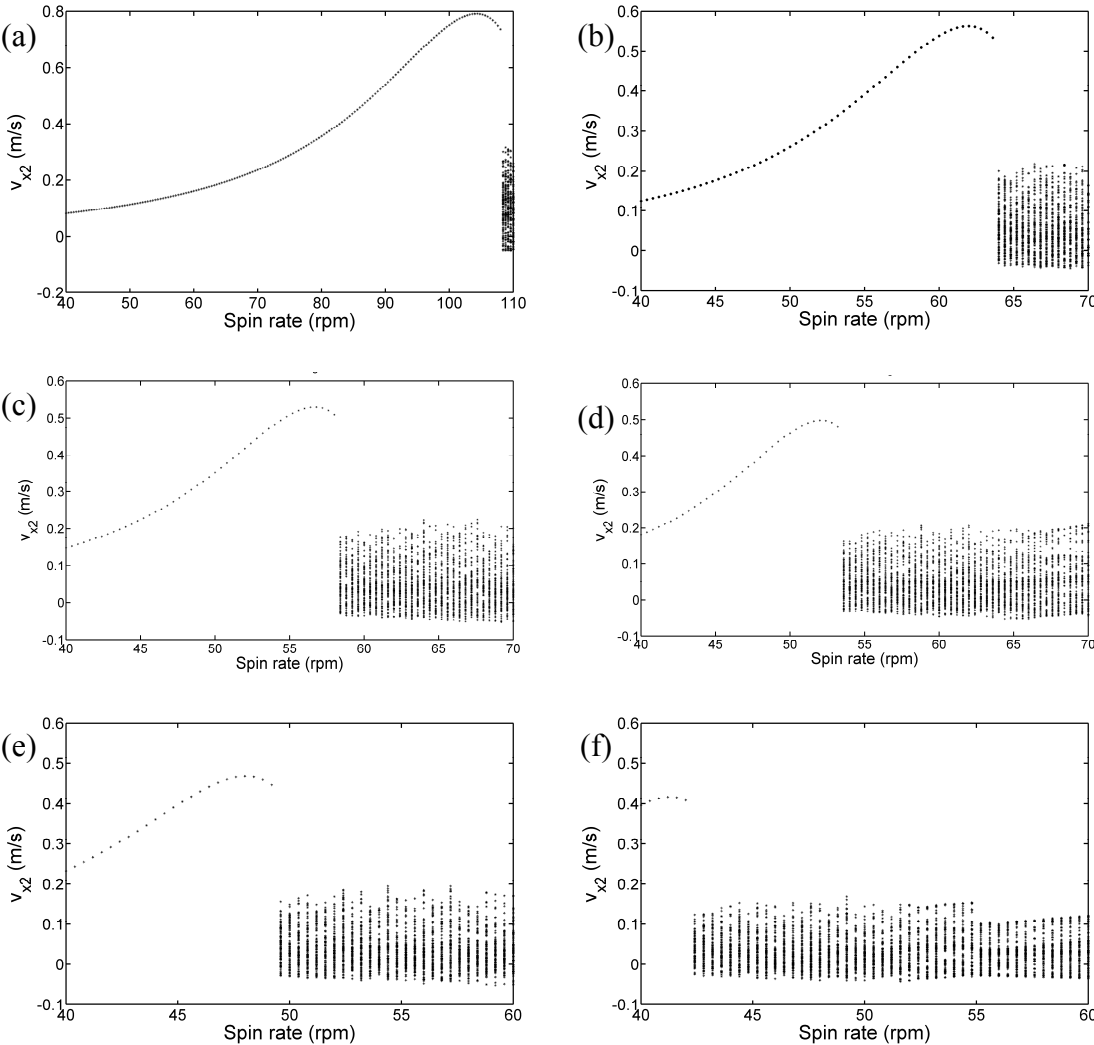


Figure 4.12. Bifurcation diagrams for model with different lengths of drill collar section (a) 15m (b) 20m (c) 21m (d) 22m (e) 23m and (d) 25m.

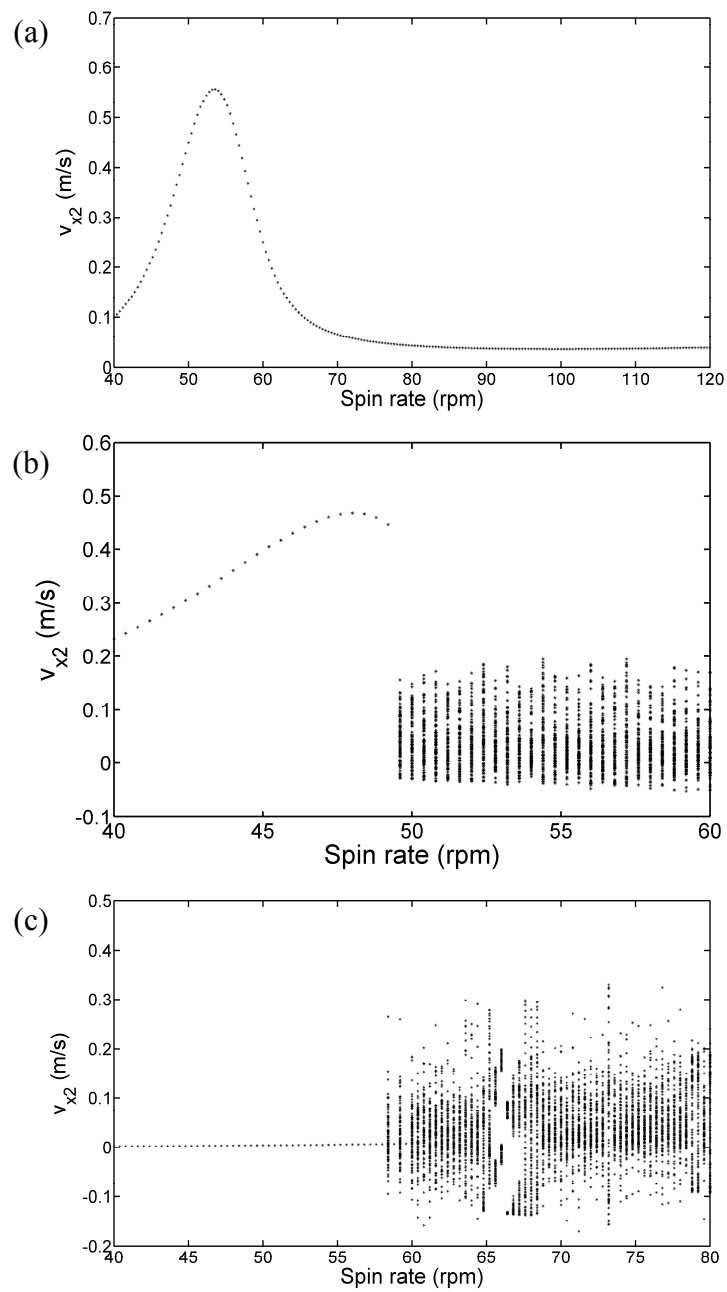


Figure 4.13. Bifurcation diagrams when varying stabilizer clearance

(a) 0.0127, (b) 0.0254 and (c) 0.0508 meters.

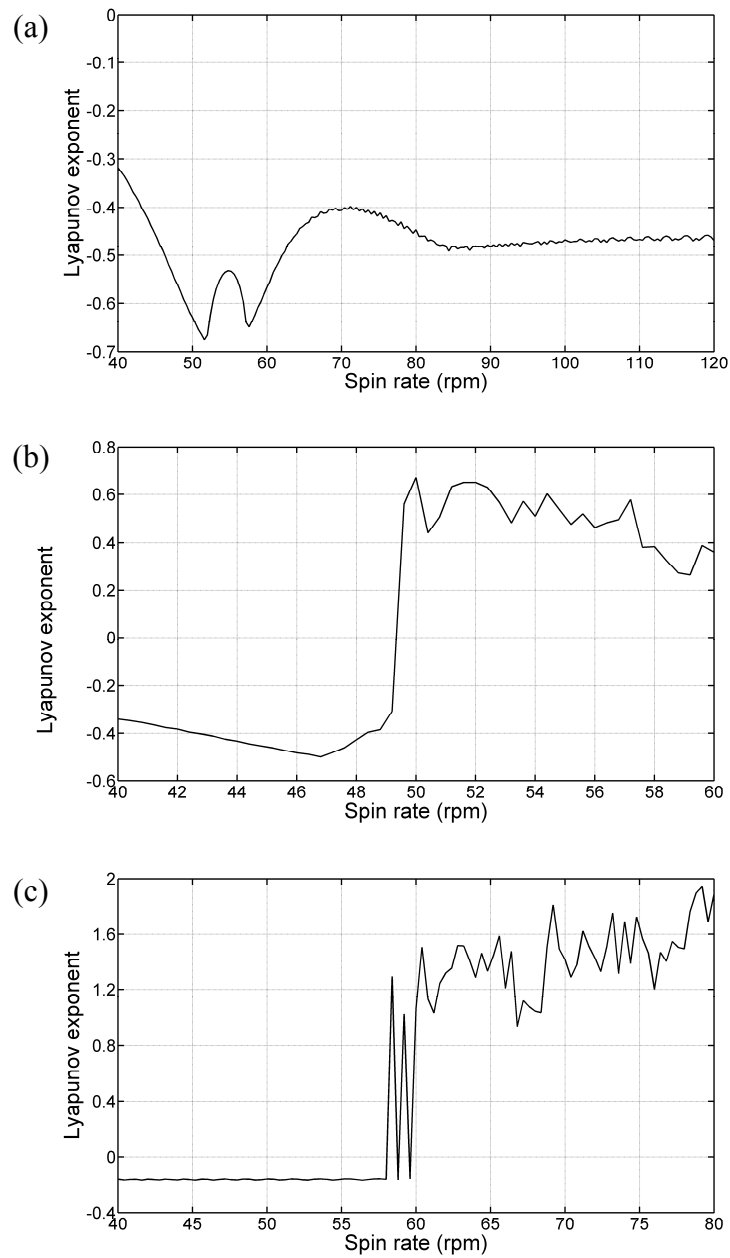


Figure 4.14. Maximum Lyapunov exponent versus drillstring rpm when varying stabilizer clearance (a) 0.0127, (b) 0.0254 and (c) 0.0508 meters.

Figures 4.15 and 4.16 show the responses for a non-chaotic and chaotic rpm after 2000 revolutions to insure steady state. The model parameters for these figures are:

$$L = 23 \text{ m}, \mu_b = 0.2, s_0 = 2.54 \text{ cm}$$

$$\text{rpm} = 45 \text{ (non-chaotic)}, \text{rpm} = 55 \text{ (chaotic)}$$

Figure 4.15(a) shows the transverse displacement response at the center of drill collar. The response is seen to be sinusoidal and stable at 45 rpm. Figure 4.15(b) shows the Poincaré map with a fix point. Figure 4.15(c) shows the frequency spectrum. It appears a single peak at 0.75 Hz which is the same frequency as the rotational frequency. Figure 4.15(d) shows that the maximum Lyapunov exponent converges to a negative value indicating a non-chaotic response.

Figure 4.16(a) shows the transverse displacement response at the drill collar midspan. The response is seen to be chaotic at 55 rpm. Figure 4.16(b) shows a Poincaré plot for transverse velocity vibration at the drill collar midspan. Sixty thousand points are plotted forming a strange attractor. This is a clear indication of chaos since the two dimensional, area type structure of the strange attractor is indicative of chaos whereas a closed line type structure indicates a quasi-periodic type of response. Figure 4.16(c) shows the frequency spectrum and appears a broad spectrum of frequencies. Figure 4.16(d) shows the maximum Lyapunov exponent convergence with time. The maximum Lyapunov exponent is positive indicating chaos.

From Figures 4.15 and 4.16, the Lyapunov exponent analysis has correctly identified both non-chaotic and chaotic responses.

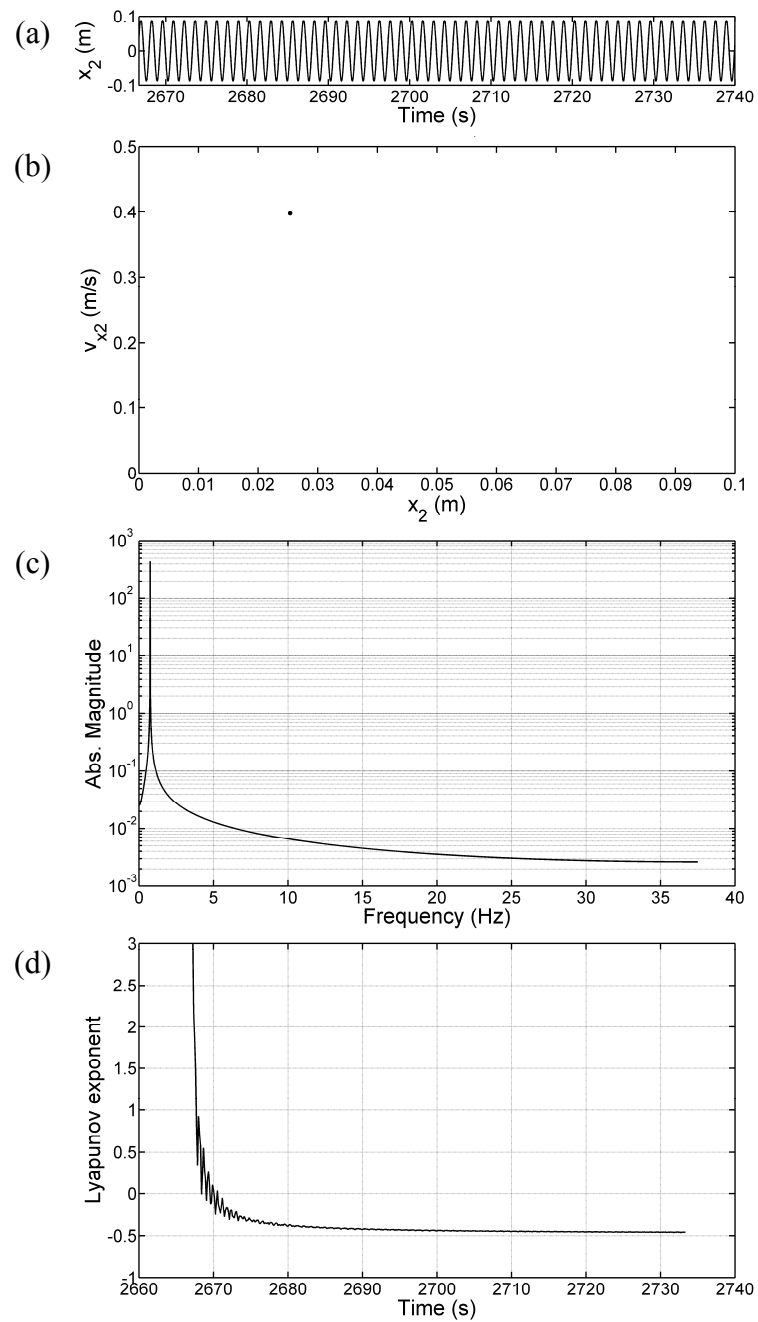


Figure 4.15. Vibration response and nonlinear dynamics analysis for a non-chaotic rpm (a) Time response (b) Poincaré map (c) frequency spectrum and (d) maximum Lyapunov exponent.

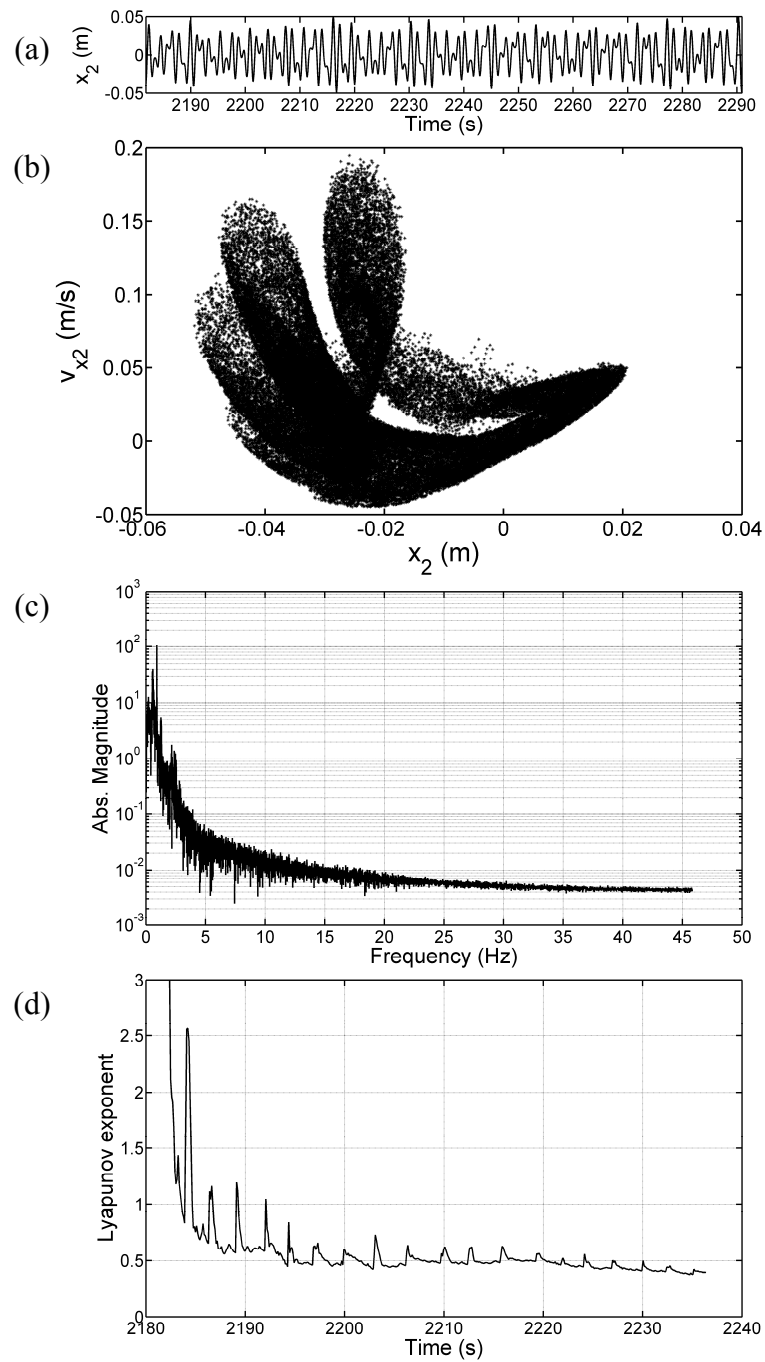


Figure 4.16. Vibration response and nonlinear dynamics analysis for a chaotic rpm (a) Time response (b) Poincaré map (c) frequency spectrum and (d) maximum Lyapunov exponent.

CHAPTER V

CONCLUSIONS

The work presented a systematic approach for predicting and analyzing the lateral vibration response of the drill collar / BHA. A lateral degree of freedom is assumed at the bit. This is a reasonable assumption because of oversize cutting (bit walk, runout, and formation swell compensation) which leaves a clearance between the bit-through diameter and the as drilled gage hole. This condition is consistent with a free bottom-end boundary condition and de-coupling of the lateral vibration from the torsional and axial vibrations. Conclusions drawn from the study include:

- 1) Neglect of the drillpipe at the upper boundary of the drill collar is a reasonable approximation for lateral vibration modeling of the drill collar – BHA component under rotating, light bit contact conditions.
- 2) Stress stiffening effects should be included in the model to account for the vertical gravity load. This is manifested in the non-zero rigid body pendulum mode.
- 3) The accuracy of the solution from the finite element model improves as the number of elements increases but the computational time also increases. The convergence of the natural frequencies is studied to evaluate the number of elements. The natural frequencies are found to converge with 10 elements for this model.
- 4) The simulation times are considered excessive to employ physical coordinate for this study. Thus modal coordinates are employed. This required selection of the number and types of modes to utilize for convergence. Both rigid body and flexible modes are included in order to produce both types of behavior in the system response. The bifurcation diagrams are found to converge with 10 modes.
- 5) The Lyapunov exponents are obtained via an averaging approach which depends on the length of time to steady state, the number of time intervals that are utilized

and the length of these time intervals. Convergence studies are conducted to determine the appropriate values for these three factors. Accurate Lyapunov exponents required approximately 2000 revolutions to reach steady state and approximately 500 time intervals to evaluate divergence/convergence of linearized solutions, with each interval approximately 0.1 revolutions in duration.

- 6) Physical parameters and other nonlinear effects shift natural frequencies from their free or constrained values so that resonance peaks occur away from the linear natural frequency values.
- 7) The nonlinear forces: a quadratic damping, and friction forces between the stabilizer and wellbore have the effect on the chaos onset speed and response amplitudes. The clearance between the stabilizer and wellbore is sufficient to cause bifurcation and chaos.
- 8) The onset speed (rpm) for chaos is shown to be significantly affected by friction, drill collar length and stabilizer-wellbore clearance. This chaos onset speed is indicated by a zero crossing of the maximum Lyapunov exponent.

The chaos onset speed decreases as the coefficient of friction and drill collar length increase. The small clearance between the stabilizer and wellbore may mitigate the occurrence of chaos.

- 9) Converged maximum Lyapunov exponents can be determined even for a system model containing many degrees of freedom such as the multi degree of freedom, modal model utilized here. The Lyapunov exponents provide a reliable indicator of chaos as confirmed by comparison with bifurcation diagrams, Poincaré plots, frequency spectrum and time solutions.

Some recommendations for future work are as follow:

- 1) The model will include lateral-torsional-axial coupling and be capable of showing the stick-slip oscillations and bit-bounce. Lyapunov exponents will then be applied to indicate the stick-slip chaos.

The coupling between lateral and torsional vibrations may reduce chaos. The torsional degree of freedom directly affects the imbalance force. If the stabilizer sticks to the wellbore, the rotational speed and also the imbalance become zero. The stabilizer then may not remain at the wellbore and the chaos will not exist.

- 2) The model will include the effects of PDC or roller cone bit and drive dynamics. The friction and the formation profile at the bit as well as effects from different types of drill bit will be included.
- 3) The experimental set-up will be built to compare the results with the simulations.

REFERENCES

- [1] Azar, A.A., and Samuel, G.R., 2007, *Drilling Engineering*, Penn Well Corporation, Tulsa, Oklahoma.
- [2] Bourgoyne Jr., A.T., Millheim, K.K., Chenevert, M.E., and Young Jr., F.S., 2005, *Applied Drilling Engineering*, Society of Petroleum Engineers, Richardson, Texas.
- [3] Rabia, H., 1985, *Oilwell Drilling Engineering: Principles and Practice*, Graham & Trotman, Gaithersburg, Maryland.
- [4] Mihajlović, N., Van Veggel, A.A., Van de Wouw, N., and Nijmeijer, H., 2004, "Analysis of Friction-Induced Limit Cycling in an Experimental Drill-String System," *ASME Journal of Dynamic Systems, Measurement, and Control*, **126** (4), pp. 709-720.
- [5] Leine, R.I., Van Campen, D.H., and Keultjes, W.J.G., 2002, "Stick-Slip Whirl Interaction in Drillstring Dynamics," *ASME Journal of Vibration and Acoustics*, **124** (2), pp. 209-220.
- [6] Lin, Y.Q., and Wang, Y.H., 1991, "Stick-Slip Vibration of Drill String," *ASME Journal of Engineering for Industry*, **113** (1), pp. 38-43.
- [7] Brett, J.F., 1992, "The Genesis of Torsional Drillstring Vibrations," *SPE Drilling Engineering*, **7**, pp. 168-174.
- [8] Cull, S.J., and Tucker, R.W., 1999, "On the Modelling of Coulomb Friction," *Journal of Physics A-Mathematical and General*, **32** (11), pp. 2103-2113.

- [9] Navarro-López E.M., and Cortés, D., 2007, "Avoiding Harmful Oscillations in a Drillstring through Dynamical Analysis," *Journal of Sound and Vibration*, **307** (1-2), pp. 152-171.
- [10] Jansen, J.D., 1991, "Non-Linear Rotor Dynamics as Applied to Oilwell Drillstring Vibrations," *Journal of Sound and Vibration*, **147** (1), pp. 115-135.
- [11] Van der Heijden, G.H.M., 1992, "Bifurcation and Chaos in Drillstring Dynamics," *Chaos, Solitons & Fractals*, **3** (2), pp. 219-247.
- [12] Kotsonis, S.J., and Spanos, P.D., 1997, "Chaotic and Random Whirling Motion of Drillstring," *ASME Journal of Energy Resources Technology*, **119**, pp. 217-222.
- [13] Yigit, A.S., and Christoforou, A.P., 2000, "Coupled Torsional and Bending Vibrations of Actively Controlled Drillstrings," *Journal of Sound and Vibration*, **234** (1), pp. 67-83.
- [14] Yigit, A.S., and Christoforou, A.P., 1996, "Coupled Axial and Transverse Vibrations of Oilwell Drillstrings," *Journal of Sound and Vibration*, **195** (4), pp. 617-627.
- [15] Richard, T., Germy, C., and Detournay, E., "Self-Excited Stick-Slip Oscillations of Drill Bits," *Comptes Rendus Mecanique*, **332** (8), pp. 619-626.
- [16] Zamanian, M., Khadem, S.E., and Ghazavi, M.R., 2007, "Stick-Slip Oscillations of Drag Bits by Considering Damping of Drilling Mud and Active Damping System," *Journal of Petroleum Science and Engineering*, **59** (3-4), pp. 289-299.

- [17] Yigit, A.S., and Christoforou, A.P., 2006, "Stick-Slip and Bit-Bounce Interaction in Oil-Well Drillstrings," *ASME Journal of Energy Resources Technology*, **128** (4), pp. 268-274.
- [18] Elsayed, M.A., Dareing, D.W., and Vonderheide, M.A., 1997, "Effect of Torsion on Stability, Dynamic Forces, and Vibration Characteristics in Drillstring," *ASME Journal of Energy Resources Technology*, **119** (1), pp. 11-19.
- [19] Christoforou, A.P., and Yigit, A.S., 2003, "Fully Coupled Vibrations of Actively Controlled Drillstrings," *Journal of Sound and Vibration*, **267** (5), pp. 1029-1045.
- [20] Melakhessou, H., Berlioz, A., and Ferraris, G., 2003, "A Nonlinear Well-Drillstring Interaction Model," *ASME Journal of Vibration and Acoustics*, **125** (1), pp. 46-52.
- [21] Detournay E., and Defourny, P., 1992, "A Phenomenological Model for the Drilling Action of Drag Bits," *International Journal of Rock Mechanics and Mining Sciences & Geomechanics Abstracts*, **29** (1), pp. 13-23.
- [22] Jogi, P.N., Macpherson, J.D., and Neubert, M., 2002, "Field Verification of Model-Derived Natural Frequencies of a Drill String," *ASME Journal of Energy Resources Technology*, **124** (3), pp. 154-162.
- [23] Spanos, P.D., Sengupta, A.K., Cunningham, R.A., and Paslay, P.R., 1995, "Modeling of Roller Cone Bit Lift-Off Dynamics in Rotary Drilling," *ASME Journal of Energy Resources Technology*, **117** (3), pp. 197-207.

- [24] Spanos, P.D., Payne, M.L., and Secora, C.K., 1997, "Bottom Hole Assembly Modeling and Dynamics Response Determination," *ASME Journal of Energy Resources Technology*, **119** (3), pp. 153-158.
- [25] Khulief, Y.A., Al-Sulaiman, F.A., and Bashmal, S., 2007, "Vibration Analysis of Drillstrings with Self-Excited Stick-Slip Oscillations," *Journal of Sound and Vibration*, **299** (3), pp. 540-558.
- [26] Reddy, J.N., 2006, *An Introduction to the Finite Element Method*, McGraw-Hill Higher Education, New York.
- [27] Cook, R.D., Malkus, D.S., Plesha, M.E., and Witt, R.J., 2002, *Concepts and Applications of Finite Element Analysis*, John Wiley & Sons, New York.
- [28] Thomson, W.T., and Dahleh, M.D., 1998, *Theory of Vibration with Applications*, Prentice Hall, Upper Saddle River, New Jersey.
- [29] Jordan, D.W., and Smith, P., 2007, *Nonlinear Ordinary Differential Equations an Introduction to Dynamical Systems*, Oxford University Press, New York.
- [30] Hilborn, R.C., 2000, *Chaos and Nonlinear Dynamics: An Introduction for Scientists and Engineers*, Oxford University Press, New York.
- [31] Wolf, A., Swift, J.B., Swinney, H.L., and Vastano, J.S., 1985, "Determinating Lyapunov Exponents from a Time Series," *Physica* **16D**, pp. 285-317.
- [32] Nayfeh, A.H., and Balachandran, B., 1995, *Applied Nonlinear Dynamics: Analytical, Computational, and Experimental Methods*, John Wiley & Sons, New York.

- [33] Moon, F.C., 1992, *Chaotic and Fractal Dynamics: An Introduction for Applied Scientists and Engineers*, John Wiley & Sons, Inc, New York.
- [34] Blevins, R.D., 1979, *Formulas for Natural Frequency and Mode Shape*, Van Nostrand Reinhold Company Inc., New York.

VITA

Name: Kathira Mongkolcheep

Address: Department of Mechanical Engineering
c/o Dr. Alan Palazzolo or Dr. Annie Ruimi
Texas A&M University
College Station, TX 77843-3123

Email Address: k.mongkolcheep@gmail.com

Education: B.Eng., Automotive Engineering, Chulalongkorn University, May
2005
M.S., Mechanical Engineering, Texas A&M University, August, 2009